Article

Cell Host & Microbe

Epithelial cells provide immunocompetence to the early embryo for bacterial clearance

Graphical abstract

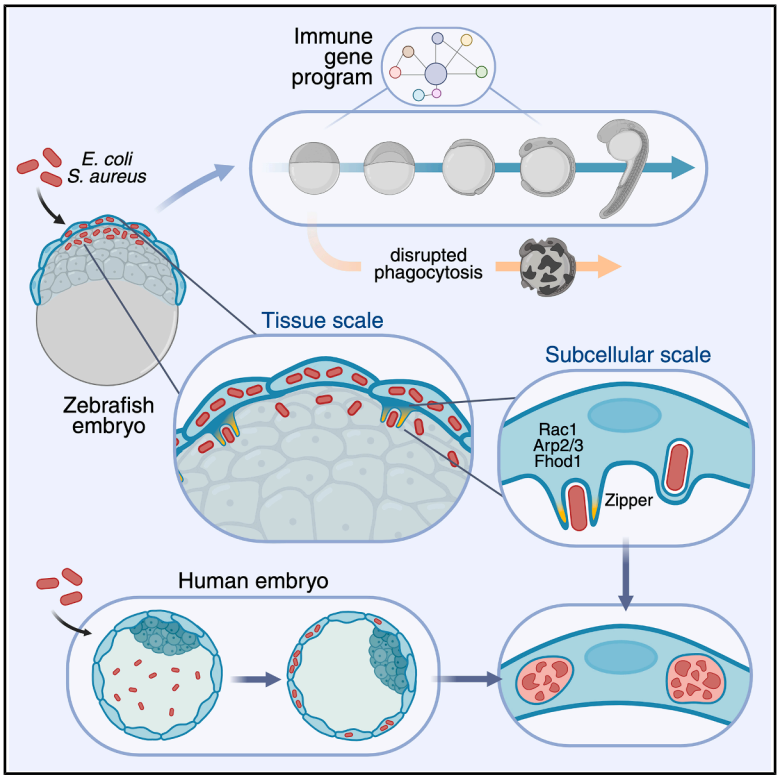

Highlights

- Early zebrafish embryos detect, engulf, and destroy commensal and pathogenic bacteria
- Clearance is performed by epithelial cells via actin-dependent zippering protrusions
- Bacteria induce an immune program on epithelial cells crucial for normal development
- Phagocytosis of bacteria is conserved in mouse and human embryos

Authors

Joan Roncero-Carol, June Olaizola-Muñoa, Begoña Arán, ..., Anna Veiga, Manuel Irimia, Esteban Hoijman

Correspondence

ehkbmc@ibmb.csic.es

In brief

Roncero-Carol et al. show that early embryos eliminate bacteria via phagocytosis by epithelial cells. Quantitative live imaging across scales in zebrafish embryos reveals an epithelial immune program essential for development. This phagocytic clearance is conserved in mouse and human embryos, highlighting an innate defense at the onset of development.

Roncero-Carol et al., 2025, Cell Host & Microbe *33*, 1106–1120
July 9, 2025
https://doi.org/10.1016/j.chom.2025.05.025

CellPress

CellPress
OPEN ACCESS

Cell Host & Microbe

Article

Epithelial cells provide immunocompetence to the early embryo for bacterial clearance

Joan Roncero-Carol,[1] June Olaizola-Muñoa,[2] Begoña Arán,[1,3,4] Loris Sebastiano Mularoni,[4] Marta Miret Cuesta,[5,6] Nuria Blanco-Cabra,[7,8] Marc Casals,[7] Mireia Rumbo,[5] Miquel Solé Inarejos,[9] Samuel Ojosnegros,[7] Berta Alsina,[5] Eduard Torrents,[7,8] Anna Veiga,[1,3,4] Manuel Irimia,[5,6,10] and Esteban Hoijman[1,2,11,*]

[1]Regenerative Medicine Program, Bellvitge Biomedical Research Institute (IDIBELL), L'Hospitalet de Llobregat, Barcelona, Spain
[2]Molecular Biology Institute of Barcelona (IBMB), Spanish Research Council (CSIC), Barcelona Science Park, Barcelona, Spain
[3]Barcelona Stem Cell Bank, L'Hospitalet de Llobregat, Barcelona, Spain
[4]Program for advancing the Clinical Translation of Regenerative Medicine of Catalonia, P-CMR[C], L'Hospitalet de Llobregat, Barcelona, Spain
[5]Department of Medicine and Life Sciences, Universitat Pompeu Fabra, PRBB, Barcelona, Spain
[6]Centre for Genomic Regulation, The Barcelona Institute of Science and Technology (BIST), Barcelona, Spain
[7]Institute for Bioengineering of Catalonia (IBEC), The Barcelona Institute of Science and Technology, Barcelona, Spain
[8]Microbiology Section, Department of Genetics, Microbiology and Statistics, Faculty of Biology, University of Barcelona, Barcelona, Spain
[9]Dexeus Fertility, Department of Obstetrics, Gynecology and Reproductive Medicine, Hospital Universitari Dexeus, Barcelona, Spain
[10]Institució Catalana de Recerca i Estudis Avançats (ICREA), Barcelona, Spain
[11]Lead contact
*Correspondence: ehkbmc@ibmb.csic.es
https://doi.org/10.1016/j.chom.2025.05.025

SUMMARY

Early embryos are exposed to environmental perturbations that may influence their development, including bacteria. Despite lacking a proper immune system, the surface epithelium of early embryos (trophectoderm in mammals) can phagocytose defective pluripotent cells. Here, we explore the dynamic interactions between early embryos and bacteria. Quantitative live imaging of infection models developed in zebrafish embryos reveals the efficient phagocytic capability of surface epithelia in detecting, ingesting, and destroying infiltrated *E. coli* and *S. aureus*. *In vivo* single-cell interferences uncover actin-based epithelial zippering protrusions mediating bacterial phagocytosis, safeguarding developmental robustness upon infection. Transcriptomic and inter-scale dynamic analyses of phagocyte-bacteria interactions identify specific features of this epithelial phagocytic program. Notably, live imaging of mouse and human blastocysts supports a conserved role of the trophectoderm in bacterial phagocytosis. This defensive role of the surface epithelium against bacterial infection provides immunocompetence to early embryos, with relevant implications for understanding failures in human embryogenesis.

INTRODUCTION

Early embryos are exposed to external and internal perturbations that may influence their development. In humans, these factors contribute to a failure rate of approximately 30% during the first weeks of natural development.[1] Since the embryonic immune system has not yet formed and the uterus is considered immune-privileged,[2] early embryos appear particularly sensitive to environmental changes.[3] Uterine bacterial infections underlie prevalent conditions such as pelvic inflammatory disease,[4,5] which requires targeted antibiotic treatments.[6,7] The bacteria would reach the uterus by ascending from the lower reproductive tract[8–10] or may constitute a potential uterine commensal microbiota.[11] Interestingly, the presence of specific bacteria in the uterus has been suggested to be associated with defective implantation, reduced embryonic viability, and, consequently, impaired human fertility.[12–16] In adult organs, professional immune phagocytes, such as macrophages and neutrophils, eliminate bacteria through phagocytosis. How early embryos respond to bacterial exposure remains unknown.

Early mammalian embryos have a transient glycoprotein coat (zona pellucida), which is removed during hatching to allow implantation, concomitantly exposing the embryo to the uterine environment. The internal pluripotent cells of the embryo are also lined by the trophectoderm, a surface epithelium equivalent to that found in other early embryos, such as the enveloping layer (EVL) in zebrafish. These layers work as mechanical barriers, like many epithelia of adult organs, which paradoxically are also the usual route of invasion by microorganisms.[17,18] We recently revealed that the surface embryonic epithelium of zebrafish and mouse embryos has biological protective roles, eliminating defective pluripotent cells from the embryo interior by phagocytosis.[19] Interestingly, in addition to expressing phagocytic receptors for apoptotic cells, these epithelial layers express receptors

involved in bacterial recognition, such as Toll-like receptors and a full repertoire of other immune-related genes.[19,20] Here, we explore the ability of early embryos to clear bacteria.

RESULTS

The surface embryonic epithelium clears bacteria

To assess the potential of the early embryo to cope with microorganisms, we established models of bacteria challenging embryos. We took advantage of zebrafish embryos, which share phagocytic abilities with mammals,[21–26] including those in epithelial cells,[19] and are naturally exposed to a wide variety of environmental pathogens and mechanical perturbations[27] due to their external development. Drawing a parallel to microbial entry into adults, we aimed to investigate how the embryo responds to bacterial infiltration. We simulated a mechanical trauma by puncturing embryos at the blastula stage (dome, 4.5 h post-fertilization [hpf]) with a needle, creating a hole in their surface (Figure S1A). Incubating these embryos in germ-free conditions indicated that bacteria naturally present in the fish water[28] (Figure S1B) can affect development and survival (Figures S1C and S1D). To visualize infiltrated bacteria, we exposed the embryos after puncturing to live non-pathogenic, non-invasive *E. coli* (expressing the fluorescent protein mCherry; Figure 1A). We observed bacteria accumulating on the healed region of the external embryonic surface where the damage was generated (Figure 1B), but they also abundantly infiltrated the embryo interior (Figure 1B). Interestingly, we found many bacteria inside cells of the surface epithelium (EVL, Figure 1C), suggesting that, in addition to apoptotic cells, these epithelial cells can also ingest *E. coli*. Internalized bacteria by the EVL were found close (Figure 1C) but also distant (Figures S1E and S1E′) to the site of damage, covering the region where the infiltrating bacteria were found. These results suggest that the EVL can clear bacteria infiltrating the interior of the embryo, a process with potential to defend the embryo in the initial stages of development.

To better understand this process of ingestion, we developed an assay injecting bacteria into the interstitial space of the embryo interior (Figure 1D), immediately followed by time-lapse imaging of the live embryo (Figure 1E). This approach allowed us to quantitatively analyze the embryonic response to bacterial infiltration. In only 40 min, the superficial epithelial layer ingested a great number of bacteria, massively clearing them from the embryo interior (Figures 1F–1H; Video S1), with a very limited contribution from the internal cells (Figures S1F and S1G). We quantified the spatiotemporal dynamics of bacterial clearance at the cell and tissue levels (Figures 1H–1J and S1H). Internalization started just 5 min after injection and was able to reach a load of at least 33.6 ± 1.3 bacteria per cell in 40 min (Figure S1H), revealing the high efficiency of these epithelial cells for bacterial ingestion. Moreover, maps of bacteria distribution in the tissue before and after ingestion showed a good spatial correlation, also illustrating the fast response of the tissue for clearance (Figures 1I and 1J). The capacity for clearing bacteria seems to be similar for the whole epithelial layer, as injecting in different regions of the embryo led to similar clearing responses (Figure S1I). We also observed that the number of bacteria ingested per EVL cell increases with the injected load until it reaches a maximum (Figure S1J), suggesting a potential saturation point for clearance. Importantly, the infiltration of *E. coli* to the embryo interior was able to dose-dependently affect embryo development and survival (Figures S1K and S1L), suggesting that the clearance by the surface epithelium could protect the embryo against harmful bacterial infections.

To test the ability of the embryo to respond to pathogenic bacteria, we injected live *S. aureus*[29] and *P. aeruginosa*[30] expressing fluorescent proteins. The EVL also ingested these bacteria (Figures 1K–1M), which were capable of causing deleterious effects in embryogenesis (Figure S1M). This demonstrates that the early zebrafish embryo can internalize both commensal and pathogenic bacteria.

Bacterial clearance occurs by a zippering phagocytic cup protrusion

To determine whether bacterial internalization by EVL cells resulted from the phagocytosis of apoptotic cells, we expressed H2A-mCherry in the embryo, which enables the visualization of apoptotic cell fragments.[19] Bacteria and apoptotic cells did not coexist within the same EVL cell (Figure S2A), indicating that bacterial internalization occurs through independent events.

Internalization of bacteria inside cells is known to occur by two different mechanisms: (1) "trigger," membrane ruffles mediating macropinocytic-like internalization of objects present in the cell vicinity (Figure S2B); or (2) "zipper," actin-rich protruding pseudopods crawling over the bacterial surface by establishing specific molecular bonds, like phagocytic cups engulfing apoptotic cells (Figure S2B).[31] These processes are induced by specific proteins of pathogenic bacteria to invade host cells or performed by phagocytic cells to eliminate extracellular bacteria. To explore the ingestion mechanisms operating in the embryonic epithelium, we first injected fixed *E. coli* or *S. aureus* and observed that they were ingested (Figures S2C and S2D), indicating that active mechanisms from live bacteria are not essential for internalization. The ingestion process is selective, as injected fluorescent *Bacillus subtilis* (*B. subtilis*) or *Lactobacillus plantarum* (*L. plantarum*), were scarcely ingested (Figures S2E–S2I), even when we killed them before injection (Figure S2J). The five bacterial species tested suggest that selectivity is not defined by their gram status, as both gram+ (*S. aureus*) or gram− (*E. coli* and *P. aeruginosa*) were efficiently ingested. Co-injection of *E. coli* together with *B. subtilis* did not promote the ingestion of the latter one (Figures S2K and S2L), suggesting that *E. coli* ingestion is not mediated by a trigger mechanism. These results support that the recognition of components present in some bacteria promotes epithelial ingestion.

To gain a deeper understanding of how *E. coli* is ingested, we visualized the protrusive activity of EVL cells. While the apical (external) side of the epithelium was relatively inactive (Figure S3A; Video S2), we observed constitutive ruffle-like protrusions (Figure S3B; Video S2) on the basal side of the epithelium (embryo interior; Figure S3C), resembling the ones identified in macrophages.[32] Interestingly, a different and intense protrusive activity of linear filaments was induced basally when the epithelium contacted infiltrated bacteria (Figure S3D; Video S2). A transgenic line to visualize F-actin dynamics only in EVL cells[19] enabled us to directly capture individual ingestion events. We observed that basal protrusions from epithelial cells exhibited a strong association of F-actin with bacteria during ingestion (Figures 2A and S3E; Videos S2–S6), suggesting the

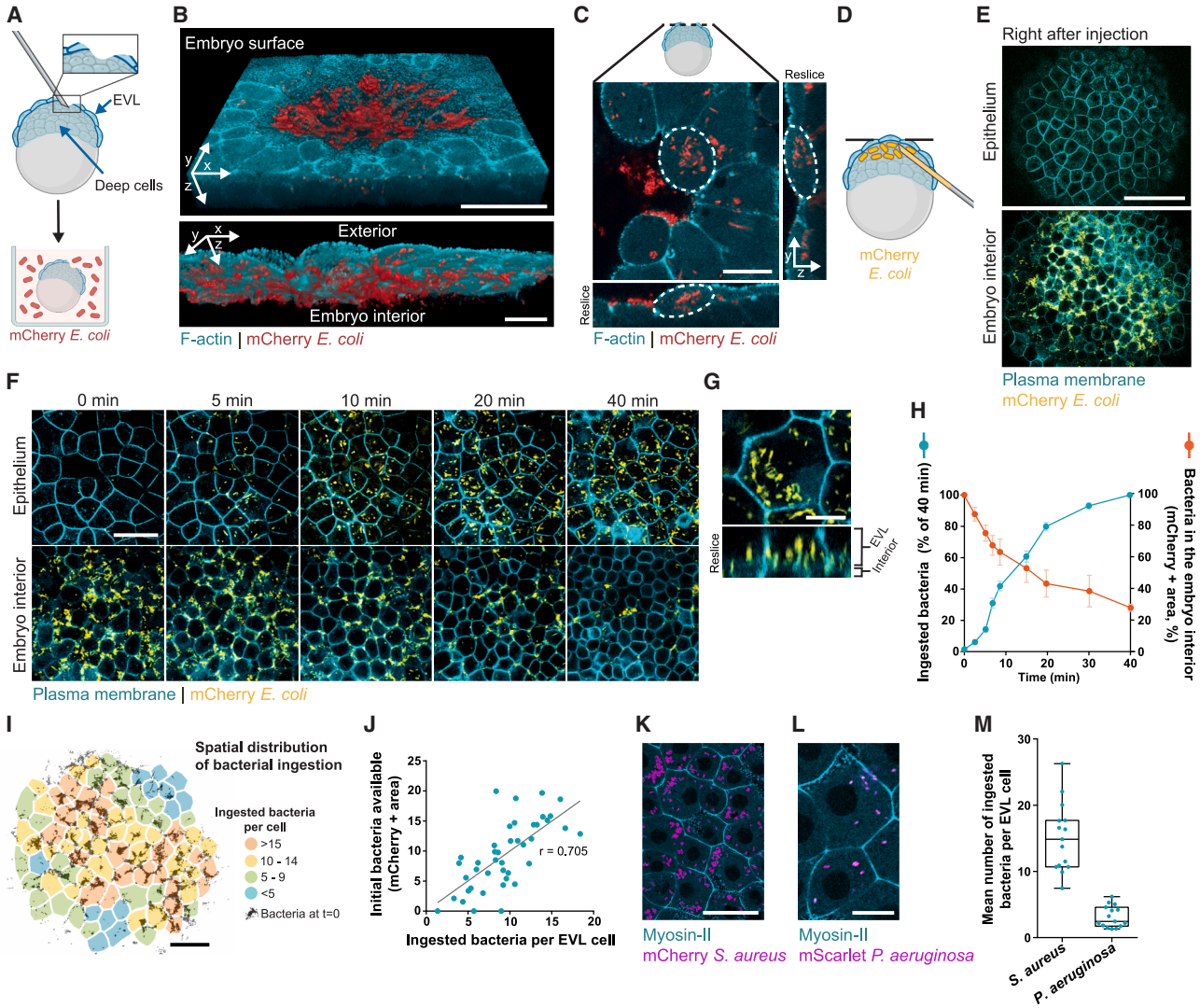

Figure 1. The surface epithelium of the early embryo clears infiltrated bacteria

(A–C) Infiltration of mCherry-expressing *E. coli* into Tg(*actb2:Lifeact-GFP*) zebrafish embryos by mechanical EVL rupture at blastula stage.
(A) Schematic of the infiltration model.
(B) 3D-reconstructed images of a harmed embryo with infiltrated bacteria.
(C) Single section and reslices showing bacteria inside epithelial cells (the dashed line indicates a single EVL cell).
(D–J) Injection at dome stage of mCherry-*E. coli* under the EVL of zebrafish embryos expressing GPI-GFP (plasma membrane).
(D) Schematic of injection model.
(E) Single slices of the EVL and the embryo interior post-injection.
(F) Time-lapse showing bacterial uptake and clearance by the EVL.
(G) Higher magnification of a single EVL cell with a high number of bacteria.
(H) Quantification of bacterial clearance dynamics (n = 5 embryos, 30 cells/embryo for ingestion; n = 4 embryos for mCherry$^+$ area). Mean ± SEM.
(I) Spatial map of *E. coli* (max z-projection, black) and epithelial cells right after injection; color-coded bacterial uptake per EVL cell at 45 min post-injection.
(J) Scatterplot showing correlation between initial bacterial exposure and uptake. Each dot corresponds to a 4-cell area (n = 172 cells, 4 embryos).
(K–M) Uptake of mCherry-*S. aureus* and mScarlet-*P. aeruginosa* by Tg(*actb2:Myl12.1-eGFP*) epithelium. EGFP signal localizes to cell junctions.
(K and L) Representative images.
(M) Quantification (n = 15 embryos/group, 20 cells/embryo). Boxplots: minimum-maximum (whiskers), medians (line), 25th–75th percentiles (boxes).
Scale bars, 50 μm (B top, F, I, and K), 20 μm (B bottom, C, and G), 100 μm (E), and 10 μm (L).
See also Figure S1.

presence of actin-dependent protrusions for the internalization of these targets. Each bacterium can be ingested individually, as visualized by the intermingling of actin between multiple bacteria (Figures 2A–2A″; Video S3), leading us to observe individual bacteria inside the EVL after ingestion (Figure 2A). Occasionally, each protrusion surrounds multiple bacteria simultaneously (Figures S3E–S3E″; Video S4), engulfing them collectively, and leading them to remain altogether after ingestion (Figures S3E′

CellPress
OPEN ACCESS

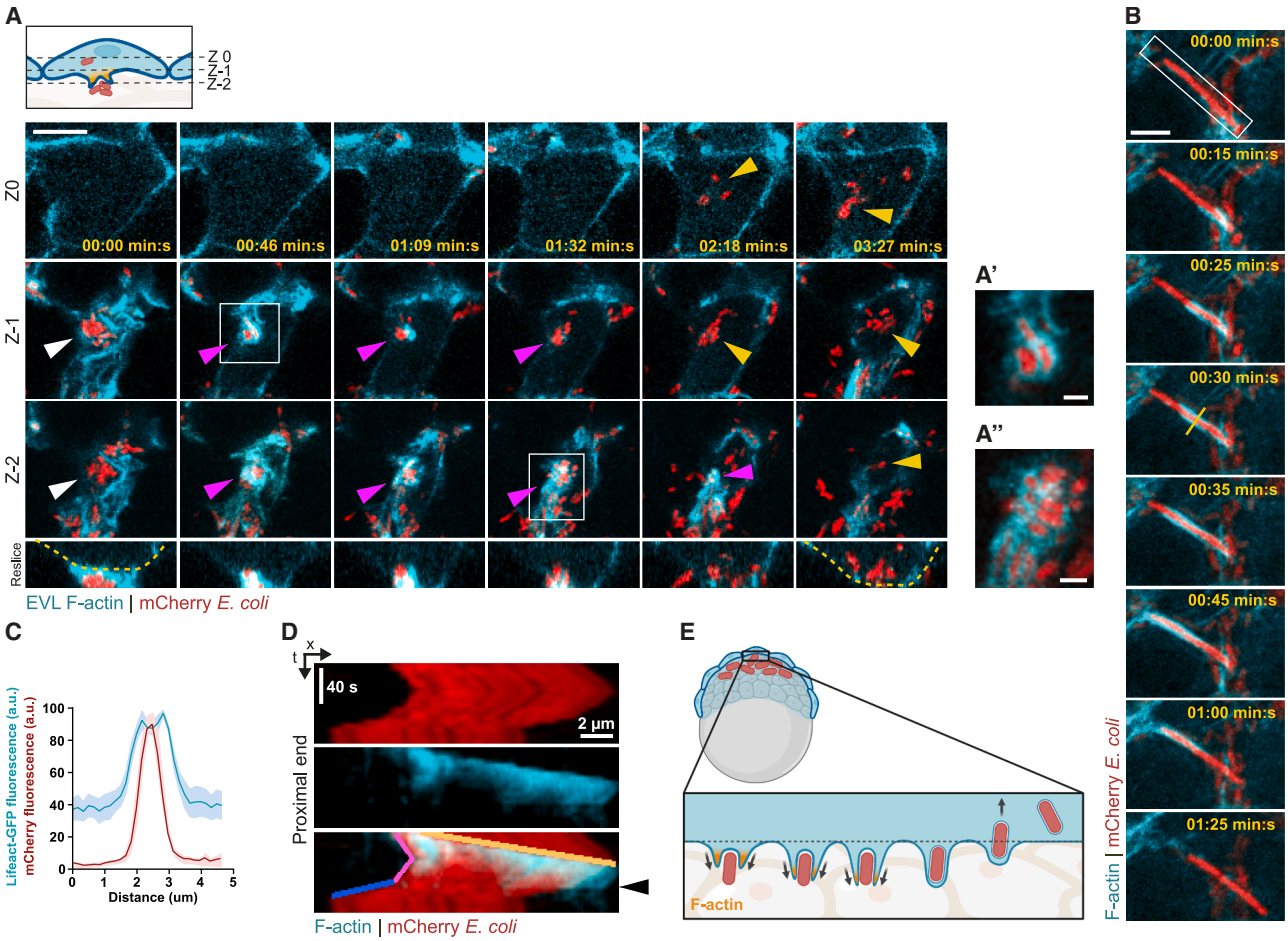

Figure 2. Protrusion dynamics for phagocytosis of bacteria by the embryonic epithelium

(A) Time-lapse of *E. coli* uptake in Tg(*krt18:Gal4FF/UAS:Lifeact-GFP*) embryos. Arrowheads indicate bacteria before (white), during (magenta), and after (yellow) ingestion. Slices at different z-planes and a reslice are shown. Insets (A′) and (A″) show close ups of actin intermingling with single bacteria during uptake. Section orientation scheme, top left.

(B) Max z-projection of a phagocytic cup in a Tg(*actb2:Lifeact-GFP*) embryo. Yellow line: section used in (C); rectangle: region for kymograph in (D).

(C) Fluorescence profiles of Lifeact-GFP and mCherry-*E. coli* (n = 5 events). Mean ± SEM.

(D) Kymograph from B, showing relative movements of F-actin and bacterium. Magenta: movement of proximal bacterial end while being wrapped by actin; blue: fast movement after actin disassembly (black arrow); yellow: actin displacement.

(E) Model of phagocytic cup dynamics: bacterial entry into the cell interior only after actin disassembly.

Scale bars, 5 µm (A) and 2 µm (A′, A″, and B).

See also Figures S2 and S3.

and S3E″; Video S4). These findings suggest a specific interaction of actin protrusions with the bacterial surface, resulting in the formation of vesicles containing either single or multiple bacteria in their interior.

The close association of actin protrusions with the bacterial surface suggests the presence of a zipper process. Taking advantage of occasional long filamentous bacteria, we analyzed their dynamic interaction with actin protrusions at a higher spatiotemporal resolution. We detected the presence of actin dynamically advancing over the bacterial surface during ingestion (Figures 2B, 2C, and S3F; Video S5), indicative of a zippering phagocytic cup protrusion mediated by actin polymerization. We then measured the speed of actin while the cup advances along the bacterium long axis (12.7 ± 1.1 µm/min). These cups behave similarly for the ingestion of short bacteria (Video S5). Subsequently, we evaluated how phagocytic cups mechanically promote the internalization of bacteria. Studies with natural targets indicate that both apoptotic cells and bacteria "slide" inside the cup but by employing different mechanisms. Cups for apoptotic cells compress the cell equator to propel them toward the phagocytic cell body[19,33] (Figure S3G), facilitated by their low stiffness and spherical shape, presumably breaking the molecular bonds of the cup with the target. Differently, extremely long bacteria slide inside a relatively static cup[34] (Figure S3G), an internalization process that would require a dynamic flow or rearrangements of the bonds between the cup and the target. To assess whether the phagocytic events we are studying involve a sliding process, we determined the absolute and relative positions of actin in the cup and the bacterium along its long axis (Figures 2B and 2D). In a first phase, actin wraps the bacterium, which only moves

subtly and in alternative directions (Figures 2B and 2D, magenta lines), indicative of an effective immobilization of the bacteria during cup growth and suggesting the presence of stable molecular bonds between them. Interestingly, once actin disassembles from the cup (Figure 2D, black arrowhead), a second phase of rapid displacement toward the cell interior occurs (Figures 2B and 2D, blue line), representing an actin-independent step. These results indicate that the ingestion of *E. coli* by the embryo involves the complete wrapping of the bacterium before its significant movement in the direction of the phagocytic cell body (Figure 2E), discarding a sliding mechanism. Actin wrapping around bacteria was also observed during the ingestion of *S. aureus* (Figures S3H–S3J; Video S6), supporting that similar actin-dependent mechanisms are used for different bacteria.

Molecular features of bacterial clearance by the early embryo

To understand the molecular control of the zippering process in these epithelial phagocytes, we interfered with Rac1 and phosphatidylinositol 3-kinase (PI3K) function, two molecules crucial for bacterial phagocytosis by macrophages[35,36] and phagocytic cup formation in the embryonic epithelium.[19] The ubiquitous expression of a dominant-negative (dn) Rac1 protein or the pharmacological inhibition of PI3K with LY2920 impaired bacterial ingestion (Figures 3A–3C and 3F). Restricting dnRac1 expression to individual cells through mosaic injections (Figures 3G and 3H) impaired their bacterial uptake without affecting that of neighboring wild-type cells (Figure 3I), suggesting a cell-autonomous effect. Accordingly, confining dnRac1 mosaic expression to the EVL tissue using the Tg(*krt18:Gal4*) line to drive a mosaic UAS:dnRac1-GFP transgene[19] also caused cell-specific interference with bacterial uptake (Figures 3J–3L).

We also explored the role of actin nucleators known to be involved in phagocytic cup dynamics.[37] Incubating the embryos with SMIFH2 (1-(3-Bromophenyl)-5-(2-furylmethylene)-2-thioxohexahydropyrimidine-4,6-dione), a formin inhibitor, strongly impaired the ingestion of *E. coli* (Figures 3D and 3F). Consistently, expression of a dn version of Fhod1 (formin homology 2 domain containing 1), a predominant formin expressed in EVL cells at these stages (Table S1) that mediates bacterial phagocytosis,[38] also reduced phagocytic uptake (Figures 3M and 3N). The intercellular heterogeneity of dnFhod1 expression enabled us to establish that its interference with phagocytosis was expression level-dependent, further supporting a cell-autonomous effect (Figure S4A). CK666, an ARP2/3 (actin-related proteins-2/3) inhibitor, also had a significant inhibitory effect on *E. coli* ingestion (Figures 3E and 3F). These results suggest that during bacterial phagocytosis, linear nucleation by formins plays a central role in actin-mediated cup functionality, contrary to previous observations regarding the phagocytosis of apoptotic cells.[12] SMIFH2 also interfered with *S. aureus* uptake (Figures S4B and S4C), suggesting that formins play a role in the uptake of various bacteria. Fourth dimensional time-lapse imaging revealed that these interferences reduced the number of phagocytic cups formed (Figures 3O and 3P) but did not affect epithelial tissue morphology (Figures 3A–3E), identity (as indicated by activation of the promoter for the epithelial marker krt18; Figure S4D), integrity (barrier function; Figure S4E), or actin localization in the internal cells of the embryo (Figure S4F). The importance of cytoskeletal perturbations for phagocytic dynamics was also evident in their impact on bacterial removal from the embryo interior (Figure S4G). This molecular analysis further supports the observation that bacterial ingestion in the embryonic epithelium is mediated by functional phagocytic cups, which rely on a Rac1-formin-actin pathway.

We then investigated which molecules on the bacterial surface could induce the formation of epithelial phagocytic protrusions. Apoptotic cells are recognized by the embryonic epithelium through the exposure of phosphatidylserine (PS) on their surface.[19] Although phagocytosis of specific bacteria could involve a PS-mediated mechanism,[39] *E. coli* phagocytosis by EVL cells was not affected by the presence of the PS-binding protein annexin V (Figures S4H and S4I), suggesting distinct mechanisms to the ones used for recognizing apoptotic cells. Bacterial LPS (lipopolysaccharide) is involved in phagocytic uptake[40] and mediates *E. coli* internalization in intestinal epithelial cells.[17] Adding LPS to the injected bacterial mix strongly inhibited *E. coli* ingestion (Figures 3Q and 3R), with its effect being dose-dependent (Figures S4J and S4K). Given the rapid kinetics of ingestion, which occurs within minutes under control conditions, it is possible that LPS competes with bacteria for a receptor or promotes its endocytosis, thereby depleting it from the cell surface.[41] Importantly, the effect of LPS depends on the identity of the bacteria, as the uptake of *S. aureus* (a gram+ bacterium that lacks LPS) was not affected by the inclusion of LPS in the mix (Figures 3S and 3T). These results suggest that the inhibitory effect of LPS on *E. coli* uptake is likely mediated by an interference with its recognition and that different bacteria are recognized by distinct surface molecules.

Phagocytosed bacteria are processed in the lysosome

To understand how these epithelial cells process bacteria after internalization, we evaluated their transport to the lysosome for digestion, aiming to discard the escape to the cytosol performed by some pathogenic bacteria inside non-phagocytic cells. We observed the sequential co-localization of ingested bacteria with: (1) the epithelial plasma membrane (Figures 4A and 4B), (2) early phagosomes (FYVE domain-GFP[42]; Figures 4C and 4D), and (3) lysosomes (Lysotracker; Figures 4E and 4F). To test the functionality of these phagolysosomes, we used *E. coli* expressing a cytosolic fluorescent pH-sensitive protein pHLuorin.[43] Our analysis showed a decreased ratio for ingested bacteria compared with the extracellular ones (Figures 4G and 4H), indicative of the acidification of the bacterial environment, supporting their lysosomal localization. This process took less than 1 h, a comparable time to the one reported for macrophages.[44] As *E. coli* can regulate its cytosolic pH independently of the external medium in this range,[45] the shift on the signal from the reporter suggests a rupture in the integrity of the bacterial membranes. The EVL lysosomes, which initially contained individual bacteria (Figures 4E and 4I), later evolved into large, rounded vesicles containing multiple processed bacteria (Figures 4J, 4J′, and S5A). In summary, these results indicate that the embryonic epithelium can destroy bacteria after ingestion, using the phagosome-lysosome vesicular transit.

The gene repertoire of the embryo against bacterial infection

We identified multiple features of professional phagocytes in the embryonic epithelium, including ruffling, LPS-dependent phagocytosis, and digestion of bacteria. To explore the gene

CellPress
OPEN ACCESS

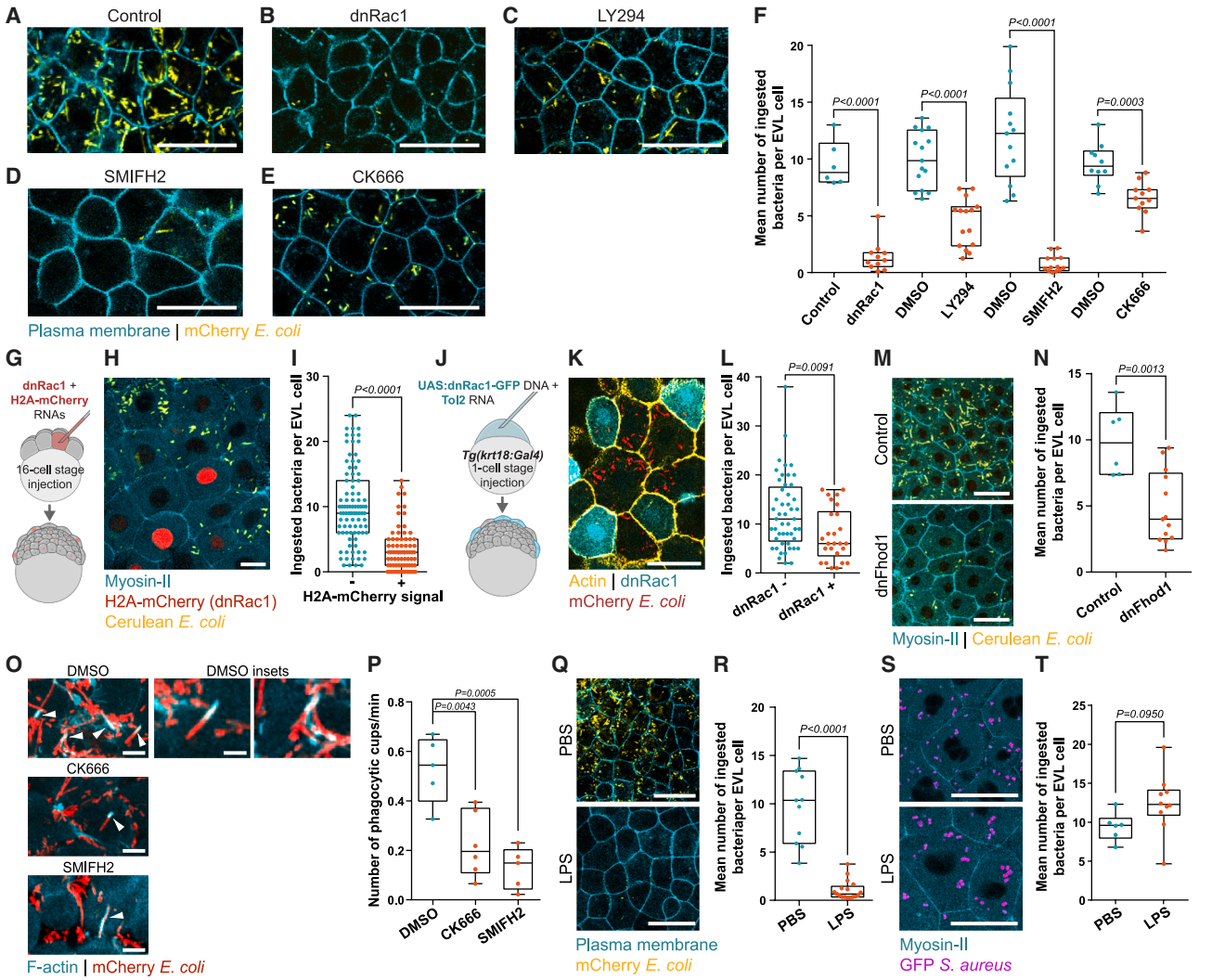

Figure 3. Molecular effectors of bacterial phagocytosis in the embryonic epithelium

(A–F) Inhibition of *E. coli* uptake 1 h after bacterial injection in GPI-GFP embryos via dnRac1 expression (B), or treatment with LY294 (C), SMIFH2 (D), or CK666 (E), compared with controls (A). (F) Quantification (n = 6–15 embryos/group, each dot corresponds to one embryo).

(G–I) dnRac1 effect on bacterial phagocytosis when expressed mosaically in the embryo.

(G) Mosaic dnRac1 expression by 16-cell stage injection tracked by H2A-mCherry.

(H) Max z-projection showing impaired uptake only in H2A-mCherry+ cells.

(I) Quantification (n = 170 cells, 8 embryos). Each dot corresponds to one cell.

(J–L) dnRac1 effect on bacterial phagocytosis when expressed exclusively in the EVL.

(J) Mosaic dnRac1 expression restricted to the EVL via UAS:dnRac1-GFP injection into a Tg(*krt18:Gal4*).

(K) Representative image; actin stained with phalloidin.

(L) Quantification per EVL cell (n = 75 cells, 5 embryos).

(M and N) Max z-projection (M) and quantification (N) of bacterial uptake in control versus dnFhod1-expressing embryos (n = 120 and 260 cells from 6 and 13 embryos for control and dnFhod1 groups, respectively).

(O and P) Effect of SMIFH2 and CK666 on actin-rich phagocytic cup formation in Tg(*actb2:Lifeact-GFP*) embryos. (O) Representative images (white arrowheads show phagocytic cups). (P) Quantification of cup number within 40 min post-injection (n = 6 embryos/group).

(Q and R) Uptake of *E. coli* resuspended in PBS or PBS + LPS in GPI-GFP embryos.

(Q) Max z-projection.

(R) Quantification (n = 11 and 17 embryos for PBS and PBS + LPS, respectively).

(S and T) Uptake of *S. aureus* resuspended in PBS or PBS + LPS in Tg(*actb2:Myl12.1-eGFP*) embryos.

(S) Max z-projection.

(T) Quantification (n = 14 and 12 embryos for PBS and PBS + LPS, respectively).

Each dot corresponds to one embryo (F, N, P, R, and T) or to one cell (I and L). Boxplots: minimum-maximum (whiskers), medians (line), 25th–75th percentiles (boxes). Unpaired two-sided t test (F, I, L, N, P, R, and T). Scale bars, 50 μm (A–E, K, M, Q, and S), 20 μm (H), 10 μm (O), and 5 μm (O insets).

See also Figure S4.

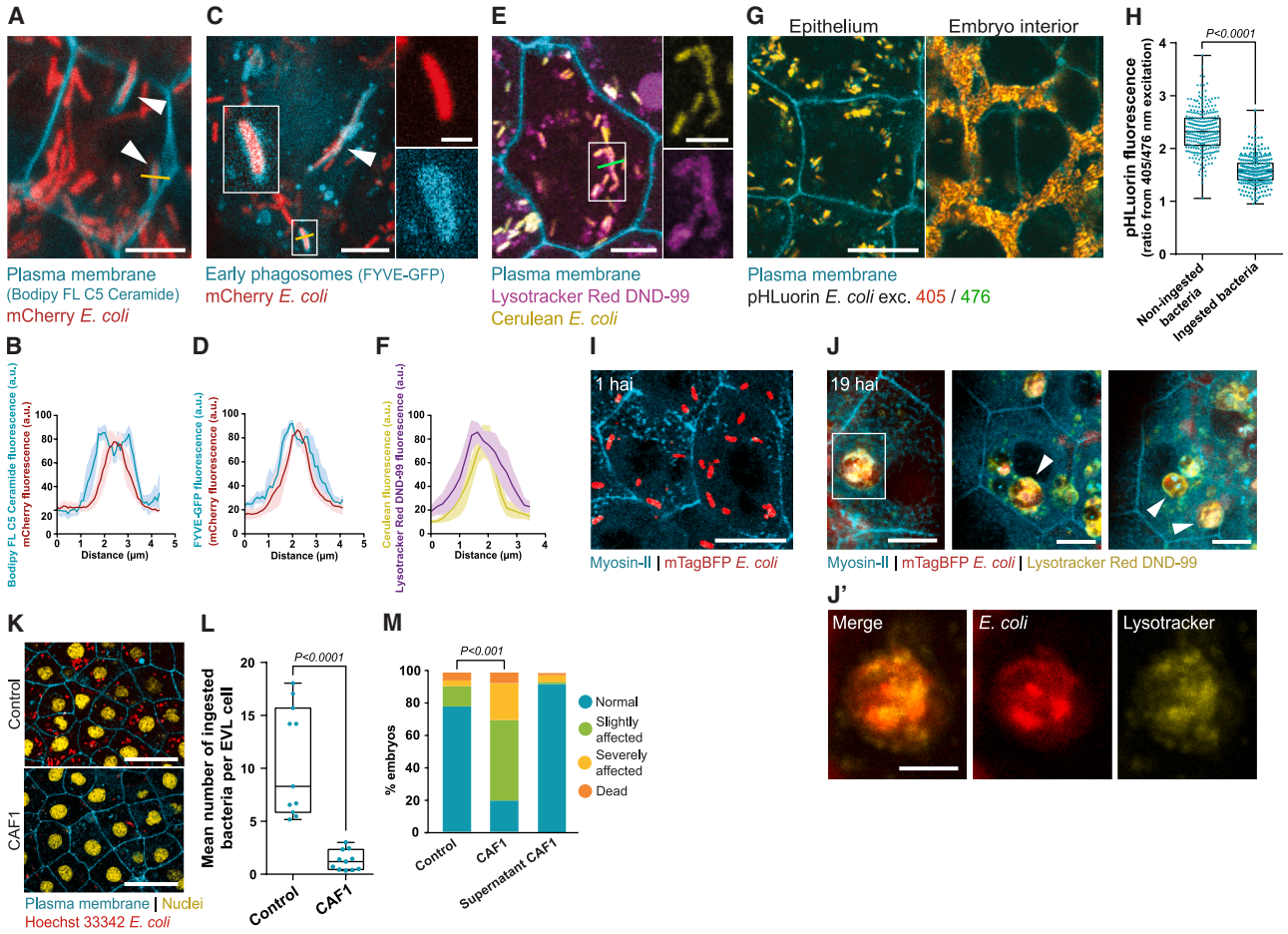

Figure 4. Vesicular transport for bacterial digestion in the embryonic epithelium

(A, C, and E) Single epithelial cell images showing phagocytic cups engulfing *E. coli* during ingestion (A, arrowheads) and early phagosomes (C) or lysosomes (E) after ingestion. White lines: representative sections used in B, D, and F. Insets show magnifications.

(B, D, and F) Fluorescence profiles quantifying bacterial position relative to membrane during ingestion (B), or within early phagosomes (D) and lysosomes (F). n = 5 events each. Mean ± SEM.

(G) Sections of the EVL and the embryo interior in a Lyn-tdTomato embryo showing ingestion of pHLuorin-*E. coli* 1 h after injection (hai). Different 405/476 emission ratios for ingested (yellow-biased) and non-ingested bacteria (red-biased) are evidenced by their different colors.

(H) Quantification of 405/476 emission ratio in pHLuorin-*E. coli* ingested or not ingested. A lower ratio indicates a lower pH. n = 286 ingested and 288 non-ingested bacteria from 9 embryos. Dots correspond to bacteria. Boxplots: minimum-maximum (whiskers), medians (line), 25th–75th percentiles (boxes). Unpaired two-sided t test.

(I–J') Max z-projections of mTagBFP2-*E. coli* 1 hai (I) or 19 hai (J). (J') Magnification of lysosomal compartments with mTagBFP2 lower fluorescence signal detected indicating accumulation of digested bacteria in EVL cells. n = 10 embryos 1 hai and 13 embryos 19 hai.

(K and L) Epithelial uptake of control (pHLuorin) or CAF1-expressing *E. coli* in Lyn-tdTomato embryos. (K) Representative images. Bacteria and EVL nuclei were stained with Hoechst 33342 (pseudo-colored in yellow). (L) Quantification of ingestion 1 hai (n = 214 and 220 cells from 11 embryos each group). Each dot corresponds to one embryo. Boxplots: minimum-maximum (whiskers), medians (line), 25th–75th percentiles (boxes). Unpaired two-sided t test.

(M) Embryo phenotype after injection with GFP-E. *coli*, CAF1-*E. coli*, or CAF1 supernatant (n = 148, 149, and 97 embryos, respectively). Means are shown. Chi-squared test.

Scale bars, 10 µm (A, C, E, and J), 2 µm (C right magnifications), 5 µm (E right magnifications, I', and J'), 20 µm (G and I), and 50 µm (K).

See also Figure S5.

program specifically activated by the interaction of this tissue with *E. coli*, we performed an RNA sequencing (RNA-seq) analysis of EVL-sorted cells from bacteria-injected or PBS-injected embryos (Figure S5B). The results (Table S1) indicate that these cells constitutively express most of the ortholog genes belonging to two reported mammalian macrophage signatures: 29/32 genes[46] and 36/40 genes[47] (6 and 3 other genes do not have orthologous identified, respectively) (Table 1), supporting that phagocytosis is a defining feature of this tissue. We found 977 genes coding for secreted proteins expressed constitutively (Table S1), including some related to innate immunity such as c3a.1, il1b, il11ra, il17d, il15, il17ra1a, tnfb, csf1a, and csf3b. Genes important for antibacterial activity were expressed in the EVL at this stage, such as pglyrp5, ifngr1, mpx, tfa, chga, acod1, duox, hmgb2, and kng1. We also found expressed several pattern recognition receptors, including tlr3, tlr4ba,

Table 1. Expression in the EVL (1.5 h after PBS injection) of genes orthologous to two macrophage gene signatures

Gautier et al.[46]		Mass et al.[47]	
Gene name from signature	Ortholog in zebrafish	Gene name from signature	Ortholog in zebrafish
Expressed in the EVL		Expressed in the EVL	
Abca1	ENSDARG00000074635	Ahnak	ENSDARG00000061764
Arsg	ENSDARG00000101715	Arid3a	ENSDARG00000070843
Camk1	ENSDARG00000029474	Asns	ENSDARG00000016375
Cd164	ENSDARG00000013628	Cmc2	ENSDARG00000043635
Comt1	ENSDARG00000015337	Dab2	ENSDARG00000053091
Ctsd	ENSDARG00000057698	Dimt1	ENSDARG00000005057
Ctsl	ENSDARG00000007836	F13a1	ENSDARG00000036893
Fert2	ENSDARG00000012196	Gria3	ENSDARG00000032737
Fgd4	ENSDARG00000101471	Guk1	ENSDARG00000030340
Glul	ENSDARG00000099776	Hba-x	ENSDARG00000069735
Lamp2	ENSDARG00000014914	Hbb-bh1	ENSDARG00000097011
Mertk	ENSDARG00000074695	Hbb-y	ENSDARG00000097011
Pecr	ENSDARG00000055976	Hp	ENSDARG00000051890
Pla2g15	ENSDARG00000103271	Id1	ENSDARG00000040764
Pla2g4a	ENSDARG00000024546	Igdcc3	ENSDARG00000075158
Pld3	ENSDARG00000068199	Mdk	ENSDARG00000036036
Plod1	ENSDARG00000059746	Mnd1	ENSDARG00000074451
Pon3	ENSDARG00000016856	Mthfd1l	ENSDARG00000042221
Ptplad2	ENSDARG00000102221	Mtx1	ENSDARG00000025500
Sepp1	ENSDARG00000093549	Nasp	ENSDARG00000039208
Sqrdl	ENSDARG00000017034	Ppat	ENSDARG00000004517
Tbxas1	ENSDARG00000002249	Raph1	ENSDARG00000006301
Tcn2	ENSDARG00000036481	Rbbp7	ENSDARG00000015208
Tlr4	ENSDARG00000019742	Recql	ENSDARG00000007175
Tmem195	ENSDARG00000025595	Rnaseh2b	ENSDARG00000005128
Tmem77	ENSDARG00000044241	Rpl35	ENSDARG00000018334
Tom1	ENSDARG00000104581	Rplp2	ENSDARG00000101406
Tpp1	ENSDARG00000042793	Rps19	ENSDARG00000030602
Tspan14	ENSDARG00000055938	Serpinh1	ENSDARG00000019949
–	–	Shox2	ENSDARG00000075713
–	–	Smc4	ENSDARG00000038882
–	–	Sptbn1	ENSDARG00000102883
–	–	Stfa1	ENSDARG00000028164
–	–	Tchp	ENSDARG00000035605
–	–	Tmsb10	ENSDARG00000077777
–	–	Tube1	ENSDARG00000096620
Low or no expression in the EVL		Low or no expression in the EVL	
Csf3r	ENSDARG00000045959	Ednrb	ENSDARG00000089334
Myo7a	ENSDARG00000044632	Mpo	ENSDARG00000019521
Tlr7	ENSDARG00000068812	Plac8	ENSDARG00000094438
–	–	Tnnt1	ENSDARG00000037954

Orthologous were not found for the genes 1810011H11Rik, Mr1, Fcgr1, A930039A15Rik, Cd14, Fcgr3 (Gautier et al.[46]) and Gm12418, Klk8, and Prtn3 (Mass et al.[47]). No information about the expression levels of Dok3 was obtained.

tlr5a, tlr5b, marco, scarb2, mincle (si:ch73-86n18.1), and dc-sign (cd209), suggesting that, similar to macrophages, multiple molecules might mediate the uptake in embryonic epithelial cells.

Focusing on early responses, we detected 486 differentially expressed genes 1.5 h after bacterial infiltration, 185 of which were upregulated (Figure S5C; Table S1). We found one module

of genes associated with nuclear factor κB (NF-κB) signaling, a key pathway related to bacterial responses in mammals and zebrafish[48,49] (Table S2; also supported by a gene set enrichment analysis [GSEA], Figure S5D). Multiple genes related to antibacterial responses were also induced (Table S1). Analysis of later responses, 9 h after bacterial infiltration, allowed us to better characterize the immune program activated in EVL cells, being 2,535 genes induced and 2,552 genes repressed by the presence of bacteria (279 of the induced genes coded for secreted proteins; Table S1). Gene Ontology (GO) analysis of induced genes detected multiple enriched terms related to immune responses (Figure S5E; Table S2). Many genes related to inflammation and antibacterial activities were induced, including tnfb, cd36, anxa1, cxcl18b, tnfsf15, irf9, cgas (LOC557043), ptger4a, c3a1, irf1a, tcim (zgc:110340), ccl19 (ccl-c5a), f2, ptgs2b (COX2), ptger2b, si:ch211-219a4.6 (parp9), sema7a, stat1, rnasel3 (angiogenin), c8a, and b2m. GO analysis of the downregulated genes indicated that, in addition to metabolic regulation, the term ''embryonic morphogenesis'' was enriched (Table S2). This includes multiple genes belonging to key developmental pathways, such as dlx5a, jag1b, neurod4, dlx3b, sema3d, ttc21b, tnika, bmp4, gdf6a, efnb1, invs, trim71, pitx2, slc26a2, sp8b, arl6, and fgfr1a suggesting that some of the defects caused by *E. coli* in development might be caused by a perturbation of these signaling pathways.

This analysis indicates that the embryonic epithelium presents some molecular similarities with innate immune cells and is therefore able to activate a set of key genes for the defense against bacterial infection.

Bacterial clearance is essential for normal development

We showed that (1) *E. coli* can induce developmental defects in early zebrafish embryos, (2) *E. coli* ingestion involves a phagocytic mechanism interacting with the bacterial surface, and (3) the surface epithelium destroys the ingested bacteria. To directly evaluate the relevance of epithelial clearance of bacteria for embryonic development, we aimed to block bacterial phagocytosis specifically and persistently. We expressed Caf1 (F1 capsule antigen) in *E. coli*, a *Yersinia pestis* protein known to form a coat around the bacterial surface that interferes with their phagocytic clearance by macrophages.[50] Similarly, expression of Caf1 in the bacteria infiltrating the embryo impaired their clearance (Figures 4K and 4L). Interestingly, these clearance-resistant bacteria generated more pronounced defects in embryonic development (Figure 4M), indicating that epithelial clearance safeguards development in the presence of bacterial infections.

Bacterial motility influences epithelial clearance

Our *in vivo* model also allowed us to test how epithelial-specific cell dynamics influence the phagocytic clearance of bacteria. While the non-motile character and stable cell-cell junctions of epithelial cells could impose limitations for phagocytic tasks, we observed high efficiency for bacterial clearance. This prompted us to investigate potential functional adaptations of this epithelium for phagocytosis. It was previously shown that bacterial motility influences the clearance efficiency of macrophages.[51,52] Even when both motile and non-motile bacteria are initially in direct contact with these targets, highly motile bacteria are cleared better due to their ability to reach phagocytic receptors.[52] This effect may be especially pronounced in epithelial phagocytes, which are morphologically constrained. Surprisingly, when we injected a combination of *E. coli* with high and low motility[53] (Mot^{HI} and Mot^{LOW}; Figures S5F and S5G) in close contact with the epithelium of the early embryo (Figure 5A), both were equally cleared (Figures 5B and 5C), having similar numbers of bacteria of each type ingested per EVL cell (Figures 5D and S5H). This experiment suggests that the short-range impact of bacterial motility on phagocytosis, which affects macrophages, does not influence clearance by these epithelial cells. However, compared with motile phagocytes such as neutrophils and certain macrophage types, epithelial tissues may have a reduced clearance capacity in conditions in which the encounter rate with bacterial targets is somehow impaired. To test this possibility, we introduced the mixture of Mot^{HI} and Mot^{LOW} 2–3 cell layers away from the epithelial layer (about 40 μm; Figure 5E), to provide time for both bacteria to move differently before ingestion. In this case, EVL cells that ingested Mot^{HI} exhibited reduced uptake of Mot^{LOW}, and vice versa (Figures 5D, 5F, and S5H), in agreement with the spatial separation of the two populations in the interior of the embryo before ingestion (Figures 5F and 5G). This result illustrates that bacterial motility can dictate the clearance pattern of static phagocytic tissues. In conjunction, these experiments indicate that this epithelial tissue is differently impacted at short and long range by target motility.

Mouse and human blastocysts ingest bacteria

To assess whether the ability of the embryonic epithelium to efficiently ingest bacteria is conserved in other epithelia, we exposed the inner ear and intestinal epithelia of zebrafish larvae to *E. coli*. These epithelia did not exhibit efficient ingestion, suggesting that the embryonic tissue possesses enhanced clearance capacities (Figures S5I and S5J). Finally, given the evolutionary conservation between zebrafish and mouse early embryos for clearing apoptotic cells,[19] we decided to test if mammalian embryos could also eliminate bacteria from the embryo interior. We injected fluorescently labeled *E. coli* (proposed to reach the uterus[54]) into the blastocoele of mouse blastocysts and found them preferentially inside the trophectoderm 8 h after injection (Figures 6A–6D). Staining with markers for the trophectoderm, pluripotent cells, and DNA confirmed the identity of the cells that internalized the bacteria and ruled out an association between bacterial uptake and apoptotic cell uptake (Figures S6A–S6C). We previously showed that both live embryonic stem cells and PS-negative lipid-coated glass beads are not ingested by the trophectoderm,[19] supporting that ingestion requires the recognition of the target surface. To prove that this is the case for *E. coli*, we coated these bacteria on glass beads and introduced them into the blastocoele. Interestingly, the coated beads were also ingested (Figures 6E and 6G), while non-coated beads were not (Figures 6F and 6G), indicating that *E. coli* drives the ingestion of glass beads by contributing with specific molecules recognized by the trophectoderm. Incubating mouse embryos with CK666 impaired bacterial uptake (Figure S6D), supporting an actin-dependent process that shares some molecular features with the zebrafish epithelium.

To assess the relevance of this ingestion in human embryos, we repeated these experiments using live imaging on donated human blastocysts. After injecting bacteria into the blastocoele (Figures 6H and 6I), we observed them inside the human trophectoderm (Figures 6J and S6E–S6G), suggesting the conservation of

CellPress
OPEN ACCESS

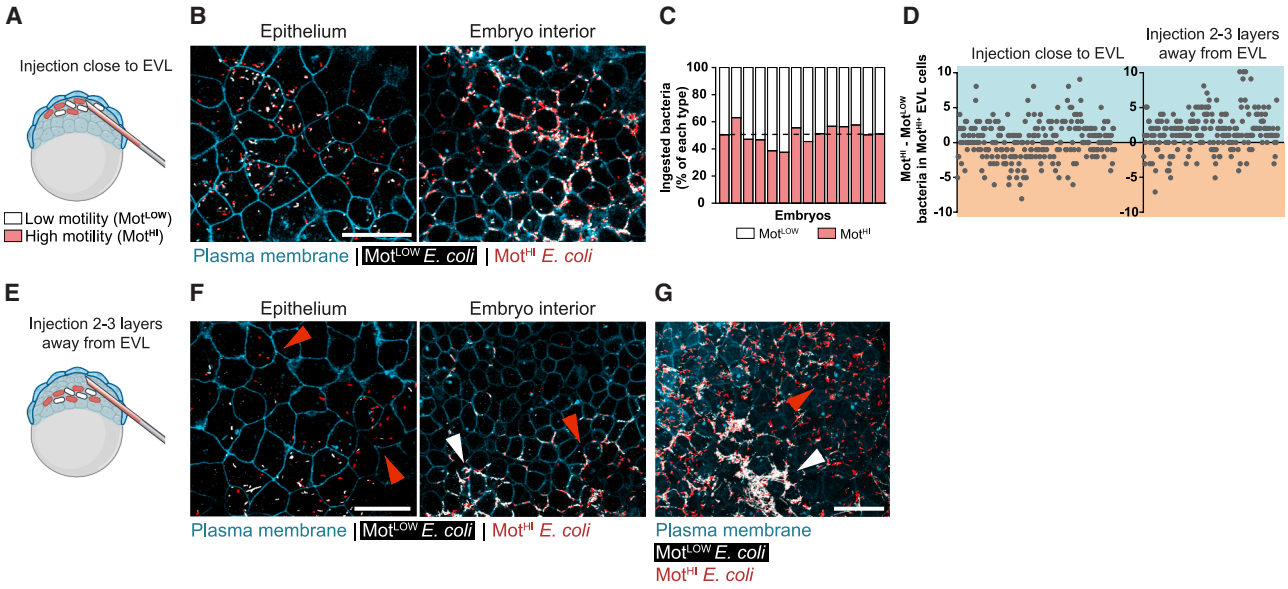

Figure 5. Motility of bacteria modulates at long range the phagocytic clearance by epithelia

(A and E) Schemes of co-injection of high- (Mot^{HI}) and low-motility (Mot^{LOW}) *E. coli* near (A) or 2–3 layers below (E) the EVL.

(B and F) Sections of Lyn-tdTomato embryos 1 hai showing YFP+ (Mot^{HI}, red) and GFP+ (Mot^{LOW}, white) *E. coli* near (B) or below (F) the EVL.

(C) Quantification of ingested Mot^{HI} versus Mot^{LOW} per embryo at the tissue level (n = 14 embryos).

(D) Difference of ingestion between Mot^{HI} and Mot^{LOW} per EVL cell. Each dot corresponds to one cell. The cells with at least one Mot^{HI} bacterium ingested are shown. n = 268 cells from 14 embryos (injection close to EVL) and 175 cells from 13 embryos (injection 2–3 layers below EVL).

(G) Max z-projection showing spatial segregation of motility variants in the embryo interior (arrowheads of each color in F and G).

Scale bars, 50 μm (B, F, and G).

See also Figure S5.

these phagocytic tasks in humans. Interestingly, *S. aureus*, a pathogenic bacterium responsible for pelvic inflammatory disease,[4] was also ingested by the human embryo (Figures 6K, 6L, and S6H), and bacterial digestion was observed (Figure S6I). These experiments show that early mammalian embryos can ingest and clear infiltrated bacteria, a defense mechanism that could provide autonomous immunocompetence at the onset of development.

DISCUSSION

Here, we show that the early embryo can effectively clear bacterial infections from its interior. Early embryos share certain mechanisms with professional phagocytes for detecting, ingesting, and destroying bacteria, including a high efficiency in various phagocytic tasks. However, they exhibit specific molecular and cellular features, such as a different dependence on target motility and the induction of a gene program possibly adapted to the embryonic context lacking in immune cells. The ability to clear both apoptotic cells and bacteria allows us to speculate that the embryo needs to establish a protective system before progressing into organ formation.

The epithelial nature of this initial protective tissue formed in development aligns with the multiple immunological roles of epithelia in adult organs.[55,56] These epithelia can perform bacterial phagocytosis, as has been reported for intestinal and pulmonary epithelia.[18] However, the exact mechanisms by which epithelial cells ingest bacteria are not well understood. Our zebrafish early embryonic model of infection allows us to explore, at different scales, the specific mechanisms used by epithelial cells to clear bacteria. We resolve the *in vivo* subcellular dynamics of actin-rich zippering phagocytic cups for *E. coli* ingestion, providing valuable insights for comparison with those used to ingest apoptotic cells.[19,33]

The reported dependence of clearance on bacterial motility relies on a hyaluronic acid coating on the macrophage surface. The absence of a hyaluronic layer[57] and other ECM (extracellular matrix) proteins[58] (Figure S5K) in the embryonic epithelium at this stage may explain the independence of epithelial clearance from bacterial motility and facilitate higher clearance efficiency. Importantly, each epithelium may present specific features and constraints. For example, embryonic and adult epithelia exhibit inverted apicobasal polarity for phagocytic tasks.[18,19] Whether the embryonic epithelium is also able to ingest bacteria from their apical side facing the embryo exterior, and a possible role for this function, still needs to be explored. In mammals, the trophectodermal barrier was shown to be disrupted during the periodic contractions of the mammalian blastocyst due to the mechanical weakening of the cell junctions,[59] an additional potential threat for the embryo. Our live bacteria-live embryo analysis at different scales can thus serve as a powerful tool to explore host-pathogen interactions involving epithelial tissues.

The ability of early embryos to eliminate bacteria changes our understanding of how embryos respond to microorganisms, revealing the potential for various cooperative, competitive, and defensive interactions. The adaptation of early embryos to their living environment may therefore shape their development. Understanding these interactions in humans could aid explaining putative associations of infertility with specific bacteria or

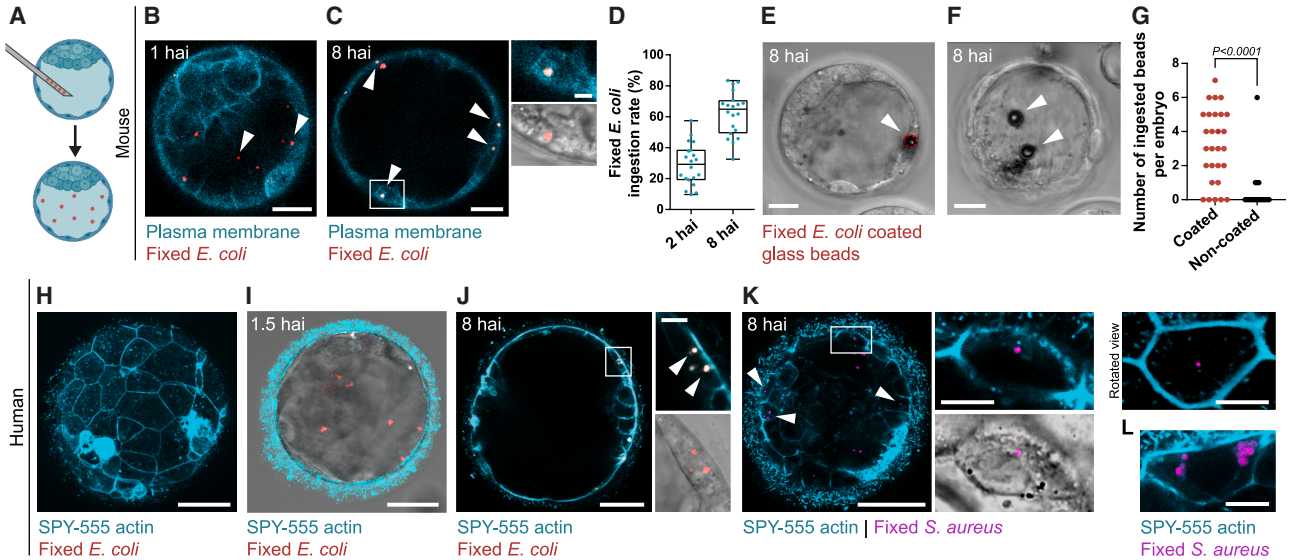

Figure 6. Mouse and human embryos clear infiltrated bacteria

(A) Scheme of bacterial injection into the blastocoel.

(B and C) TdTomato E3.5 TdTomato-expressing mouse blastocysts 1 hai (B) or 8 hai (C) of fixed *E. coli*-Texas red (arrowheads). Inset in C shows magnification of boxed area.

(D) Quantification of fixed *E. coli* ingestion by the mouse trophectoderm 2 and 8 hai (n = 20 blastocysts). Each dot corresponds to one embryo. Boxplots: minimum-maximum (whiskers), medians (line), 25th–75th percentiles (boxes). Unpaired two-sided t test.

(E and F) E3.5 mouse blastocysts injected with 9–13 μm glass beads coated (E) or not (F) with fixed *E. coli*.

(G) Quantification of bead ingestion by the trophectoderm (n = 28 blastocysts for coated, 19 for uncoated). Each dot corresponds to one embryo. Unpaired two-sided t test.

(H) Human blastocyst stained with SPY555-actin 1.5 hai of fixed *E. coli*-Texas red.

(I) Particles inside the human blastocoele 1.5 hai (red, max z-projection) and actin (cyan, single plane).

(J–L) Max z-projection showing ingestion of fixed *E. coli* (J) and *S. aureus* (K and L) by the human trophectoderm. Insets show higher magnifications and 3D reconstruction views (L). Images are representative of 5 (J) and 8 (K) embryos with similar results. The mean number of ingested bacteria per embryo was 4.3 ± 1.4 for *E. coli* and 11.4 ± 4.3 for *S. aureus*.

Scale bars, 25 μm (B, C, E, and F), 5 μm (C insets), 50 μm (H–K main), and 10 μm (J and K insets, and L).

See also Figure S6.

potential defects in embryonic clearance and contribute to the development of effective therapies. Our findings also make increasingly important to precisely define the community of invading or resident uterine bacteria.

In summary, our results support the notion that the early embryo is autonomously immunocompetent to eliminate bacterial infections long before the formation of the embryonic myeloid immune system. This self-protection may be essential for proper developmental progression, making it important to understand the relationship between microorganisms and human fertility.

Limitations of the study

Our study demonstrates the ability of early embryos to clear bacteria using various infiltration models. In humans, how these processes occur within the uterus remains unknown due to the inability to visualize preimplantation embryos *in vivo*, leaving open the possibility of diverse infiltration mechanisms. Limited data on natural early human embryo failure, along with the scarcity, heterogeneity, and brief developmental window of donated embryos, further constrains our understanding of the long-term consequences of bacterial infiltration. While defects in phagocytic clearance may contribute to unexplained infertility, this potential connection requires further investigation.

We show that bacterial uptake is conserved between zebrafish and mammals, characterized by the clearance of both commensal and pathogenic bacteria, dependence on ARP2/3, epithelial specificity, requirement for bacterial surface recognition, independence from apoptotic cell clearance, and the destruction of internalized bacteria. Whether additional molecular mechanisms are also conserved remains unknown, as does the identity of the receptors mediating bacterial recognition.

Our study also did not determine the extent to which bacterial clearance relies on maternally inherited factors versus *de novo* embryonic programs. Although our findings suggest that antibacterial responses may intersect with developmental processes, the precise coordination between these systems remains to be clarified. More broadly, embryonic defense mechanisms beyond phagocytosis—such as the production of antimicrobial peptides—remain poorly characterized and could reveal broader strategies for microbial management during early development.

RESOURCE AVAILABILITY

Lead contact

Further information and requests for resources and reagents should be directed to and will be fulfilled by the lead contact, Esteban Hoijman (ehkbmc@ibmb.csic.es).

Materials availability

This study did not generate new unique reagents.

Data and code availability

- Raw data for the RNA-seq analysis was deposited in the public repository CORA.RDR and can be accessed by the following links: CORA.RDR: https://doi.org/10.34810/data1201 and CORA.RDR: https://doi.org/10.34810/data2009.
- This paper does not report original code.
- Any additional information required to reanalyze the data reported in this paper is available from the lead contact upon request.

ACKNOWLEDGMENTS

We thank Andrés Hidalgo, Miguel Torres, and Stefanie Wculek for discussions and suggestions for the manuscript. We particularly thank Stephen Forrow, Barbara Tondelli, and Julien Colombelli from IRB, Tania García Becerra from IBMB, and Juana Fernández Rodríguez and Antoni Ventura from IDIBELL, for making possible the mouse experiments. We thank the support of the Animal facility, Bioimaging platform and Biostatistics Unit from IDIBELL, the Genomics unit from CRG, and the flow cytometry services from VHIR and the Parc Cientific of Barcelona. We thank Javier Moreno Santos for the mCherry-expressing strain, Senda Jimenez Delgado for sharing technical expertise, Nelly Henry for the bacteria with different motility, Jeff Rasmussen for the UAS-FYVE plasmid, Jan Roelof van Der Meer for the pHLuorin plasmids, Jeremy H. Lakey for the Caf1 plasmid, Shrikrishnan Sankaran for the fluorescent *L. plantarum* strains, Ákos T. Kovács for the fluorescent *B. subtilis* strains, Shang Yang for the BFP plasmid, Kayvon Pedram for the Rhobo6 dye, Verena Ruprecht for the dnFhod1 plasmid, Aitor Lavado for his assistance with the graphic design work, and Jordi Guiu, Victoriano Mulero, and Miguel Moreno Mateos for sharing resources. J.R.-C. acknowledges an FPU fellowship 22/04307 funded by Spanish Ministry of Science and Innovation and an FI fellowship 100057 from AGAUR. E.T. acknowledges funding from MCIN/AEI/10.13039/501100011033 "ERDF A way of making Europe" PID2021-125801OB-100 and AGAUR 2021SGR01545. A.V. acknowledges funding from Instituto de Salud Carlos III (PT23/00092). M.I. acknowledges funding from the Spanish Ministry of Science and Innovation (PID2020-115040GB-I00). E.H. acknowledges support from the Spanish Ministry of Science and Innovation (PID2020-117540GB-I00 and PID2023-151237NB-I00) and the AGAUR (2022-SGR-00974). E.H. held a Serra Hunter Lecturer position by the Generalitat of Catalonia at the University of Barcelona.

AUTHOR CONTRIBUTIONS

J.R.-C. designed research, performed most of the zebrafish, mouse, and human experiments, analyzed data, and contributed to writing; J.O.-M. contributed to zebrafish experiments; B. Arán contributed to human experiments; L.S.M. analyzed the RNA-seq raw data; M.M.C. and M.C. contributed to mouse experiments; N.B.-C. contributed to the zebrafish experiments involving pathogenic bacteria; M.R. contributed to interference zebrafish experiments; M.S.I. provided the donated human embryos; S.O. and B. Alsina provided resources; E.T. provided resources and supervised N.B.-C.; A.V. provided resources and supervision for human experiments; M.I. provided resources and supervision for mouse experiments and contributed to writing; E.H. conceptualized the study, designed research, supervised experiments, performed experiments and data analysis, and wrote the manuscript.

DECLARATION OF INTERESTS

The authors declare no competing interests.

STAR★METHODS

Detailed methods are provided in the online version of this paper and include the following:

SUPPLEMENTAL INFORMATION

Supplemental information can be found online at https://doi.org/10.1016/j.chom.2025.05.025.

Received: April 11, 2024
Revised: March 2, 2025
Accepted: May 23, 2025
Published: June 18, 2025

REFERENCES

1. Wilcox, A.J., Weinberg, C.R., O'Connor, J.F., Baird, D.D., Schlatterer, J.P., Canfield, R.E., Armstrong, E.G., and Nisula, B.C. (1988). Incidence of early loss of pregnancy. N. Engl. J. Med. *319*, 1483–1484. https://doi.org/10.1056/NEJM198812013192214.
2. Clark, G.F., and Schust, D.J. (2013). Manifestations of immune tolerance in the human female reproductive tract. Front. Immunol. *4*, 26. https://doi.org/10.3389/FIMMU.2013.00026.
3. Hamdoun, A., and Epel, D. (2007). Embryo stability and vulnerability in an always changing world. Proc. Natl. Acad. Sci. USA *104*, 1745–1750. https://doi.org/10.1073/PNAS.0610108104.
4. Brunham, R.C., Gottlieb, S.L., and Paavonen, J. (2015). Pelvic inflammatory disease. N. Engl. J. Med. *372*, 2039–2048. https://doi.org/10.1056/NEJMra1411426.
5. Kreisel, K., Torrone, E., Bernstein, K., Hong, J., and Gorwitz, R. (2017). Prevalence of Pelvic Inflammatory Disease in Sexually Experienced Women of Reproductive Age — United States, 2013–2014. MMWR

Morb. Mortal. Wkly. Rep. *66*, 80–83. https://doi.org/10.15585/MMWR.MM6603A3.

6. Ross, J., Guaschino, S., Cusini, M., and Jensen, J. (2017). European guideline for the management of pelvic inflammatory disease 29, 108–114. https://doi.org/10.1177/0956462417744099.
7. Workowski, K.A., Bachmann, L.H., Chan, P.A., Johnston, C.M., Muzny, C. A., Park, I., Reno, H., Zenilman, J.M., and Bolan, G.A. (2021). Sexually Transmitted Infections Treatment Guidelines, 2021. MMWR Recomm. Rep. *70*, 1–187. https://doi.org/10.15585/MMWR.RR7004A1.
8. Suff, N., Karda, R., Diaz, J.A., Ng, J., Baruteau, J., Perocheau, D., Tangney, M., Taylor, P.W., Peebles, D., Buckley, S.M.K., et al. (2018). Ascending Vaginal Infection Using Bioluminescent Bacteria Evokes Intrauterine Inflammation, Preterm Birth, and Neonatal Brain Injury in Pregnant Mice. Am. J. Pathol. *188*, 2164–2176. https://doi.org/10.1016/J.AJPATH.2018.06.016.
9. O'Brien, V.P., Gilbert, N.M., Lebratti, T., Agarwal, K., Foster, L., Shin, H., and Lewis, A.L. (2019). Low-dose inoculation of Escherichia coli achieves robust vaginal colonization and results in ascending infection accompanied by severe uterine inflammation in mice. PLOS One *14*, e0219941. https://doi.org/10.1371/JOURNAL.PONE.0219941.
10. Baker, J.M., Chase, D.M., and Herbst-Kralovetz, M.M. (2018). Uterine Microbiota: Residents, Tourists, or Invaders? Front. Immunol. *9*, 208. https://doi.org/10.3389/FIMMU.2018.00208.
11. Chen, C., Song, X., Wei, W., Zhong, H., Dai, J., Lan, Z., Li, F., Yu, X., Feng, Q., Wang, Z., et al. (2017). The microbiota continuum along the female reproductive tract and its relation to uterine-related diseases. Nat. Commun. *8*, 875. https://doi.org/10.1038/S41467-017-00901-0.
12. Chen, W., Wei, K., He, X., Wei, J., Yang, L., Li, L., Chen, T., and Tan, B. (2021). Identification of Uterine Microbiota in Infertile Women Receiving in vitro Fertilization With and Without Chronic Endometritis. Front. Cell Dev. Biol. *9*, 693267. https://doi.org/10.3389/FCELL.2021.693267.
13. Moreno, I., Garcia-Grau, I., Perez-Villaroya, D., Gonzalez-Monfort, M., Bahçeci, M., Barrionuevo, M.J., Taguchi, S., Puente, E., Dimattina, M., Lim, M.W., et al. (2022). Endometrial microbiota composition is associated with reproductive outcome in infertile patients. Microbiome *10*, 1. https://doi.org/10.1186/S40168-021-01184-W.
14. Reschini, M., Benaglia, L., Ceriotti, F., Borroni, R., Ferrari, S., Castiglioni, M., Guarneri, D., Porcaro, L., Vigano', P., Somigliana, E., et al. (2022). Endometrial microbiome: sampling, assessment, and possible impact on embryo implantation. Sci. Rep. *12*, 8467. https://doi.org/10.1038/S41598-022-12095-7.
15. Bui, B.N., van Hoogenhuijze, N., Viveen, M., Mol, F., Teklenburg, G., de Bruin, J.P., Besselink, D., Brentjens, L.S., Mackens, S., Rogers, M.R.C., et al. (2023). The endometrial microbiota of women with or without a live birth within 12 months after a first failed IVF/ICSI cycle. Sci. Rep. *13*, 3444. https://doi.org/10.1038/S41598-023-30591-2.
16. Moreno, I., Codoñer, F.M., Vilella, F., Valbuena, D., Martinez-Blanch, J.F., Jimenez-Almazán, J., Alonso, R., Alamá, P., Remohí, J., Pellicer, A., et al. (2016). Evidence that the endometrial microbiota has an effect on implantation success or failure. Am. J. Obstet. Gynecol. *215*, 684–703. https://doi.org/10.1016/J.AJOG.2016.09.075.
17. Neal, M.D., Leaphart, C., Levy, R., Prince, J., Billiar, T.R., Watkins, S., Li, J., Cetin, S., Ford, H., Schreiber, A., et al. (2006). Enterocyte TLR4 mediates phagocytosis and translocation of bacteria across the intestinal barrier. J. Immunol. *176*, 3070–3079. https://doi.org/10.4049/JIMMUNOL.176.5.3070.
18. Günther, J., and Seyfert, H.M. (2018). The first line of defence: insights into mechanisms and relevance of phagocytosis in epithelial cells. Semin. Immunopathol. *40*, 555–565. https://doi.org/10.1007/S00281-018-0701-1.
19. Hoijman, E., Häkkinen, H.M., Tolosa-Ramon, Q., Jiménez-Delgado, S., Wyatt, C., Miret-Cuesta, M., Irimia, M., Callan-Jones, A., Wieser, S., and Ruprecht, V. (2021). Cooperative epithelial phagocytosis enables error correction in the early embryo. Nature *590*, 618–623. https://doi.org/10.1038/S41586-021-03200-3.
20. Aboussahoud, W.S., Smith, H., Stevens, A., Wangsaputra, I., Hunter, H.R., Kimber, S.J., Seif, M.W., and Brison, D.R. (2021). The expression and activity of Toll-like receptors in the preimplantation human embryo suggest a new role for innate immunity. Hum. Reprod. *36*, 2661–2675. https://doi.org/10.1093/HUMREP/DEAB188.
21. Kanther, M., and Rawls, J.F. (2010). Host-microbe interactions in the developing zebrafish. Curr. Opin. Immunol. *22*, 10–19. https://doi.org/10.1016/J.COI.2010.01.006.
22. Davis, J.M., and Ramakrishnan, L. (2009). The role of the granuloma in expansion and dissemination of early tuberculous infection. Cell *136*, 37–49. https://doi.org/10.1016/J.CELL.2008.11.014.
23. Yoshida, N., Frickel, E.M., and Mostowy, S. (2017). Macrophage-Microbe Interactions: Lessons from the Zebrafish Model. Front. Immunol. *8*, 1703. https://doi.org/10.3389/FIMMU.2017.01703.
24. Yoo, S.K., Starnes, T.W., Deng, Q., and Huttenlocher, A. (2011). Lyn is a redox sensor that mediates leukocyte wound attraction in vivo. Nature *480*, 109–112. https://doi.org/10.1038/NATURE10632.
25. Huang, C., and Niethammer, P. (2016). Illuminating Phagocyte Biology: The View from Zebrafish. Dev. Cell *38*, 133–134. https://doi.org/10.1016/J.DEVCEL.2016.07.003.
26. Coombs, C., Georgantzoglou, A., Walker, H.A., Patt, J., Merten, N., Poplimont, H., Busch-Nentwich, E.M., Williams, S., Kotsi, C., Kostenis, E., et al. (2019). Chemokine receptor trafficking coordinates neutrophil clustering and dispersal at wounds in zebrafish. Nat. Commun. *10*, 5166. https://doi.org/10.1038/S41467-019-13107-3.
27. Kim, D.H., Hwang, C.N., Sun, Y., Lee, S.H., Kim, B., and Nelson, B.J. (2006). Mechanical analysis of chorion softening in prehatching stages of zebrafish embryos. IEEE Trans. Nanobiosci. *5*, 89–94. https://doi.org/10.1109/TNB.2006.875054.
28. Rawls, J.F., Samuel, B.S., and Gordon, J.I. (2004). Gnotobiotic zebrafish reveal evolutionarily conserved responses to the gut microbiota. Proc. Natl. Acad. Sci. USA *101*, 4596–4601. https://doi.org/10.1073/pnas.0400706101.
29. Hepburn, L., Prajsnar, T.K., Klapholz, C., Moreno, P., Loynes, C.A., Ogryzko, N.V., Brown, K., Schiebler, M., Hegyi, K., Antrobus, R., et al. (2014). Innate immunity. A Spaetzle-like role for nerve growth factor β in vertebrate immunity to Staphylococcus aureus. Science *346*, 641–646. https://doi.org/10.1126/SCIENCE.1258705.
30. McCarthy, R.R., Mazon-Moya, M.J., Moscoso, J.A., Hao, Y., Lam, J.S., Bordi, C., Mostowy, S., and Filloux, A. (2017). Cyclic-di-GMP regulates lipopolysaccharide modification and contributes to Pseudomonas aeruginosa immune evasion. Nat. Microbiol. *2*, 17027. https://doi.org/10.1038/NMICROBIOL.2017.27.
31. Ribet, D., and Cossart, P. (2015). How bacterial pathogens colonize their hosts and invade deeper tissues. Microbes Infect. *17*, 173–183. https://doi.org/10.1016/J.MICINF.2015.01.004.
32. Condon, N.D., Heddleston, J.M., Chew, T.L., Luo, L., McPherson, P.S., Ioannou, M.S., Hodgson, L., Stow, J.L., and Wall, A.A. (2018). Macropinosome formation by tent pole ruffling in macrophages. J. Cell Biol. *217*, 3873–3885. https://doi.org/10.1083/JCB.201804137.
33. Vorselen, D., Barger, S.R., Wang, Y., Cai, W., Theriot, J.A., Gauthier, N.C., and Krendel, M. (2021). Phagocytic "teeth" and myosin-II "jaw" power target constriction during phagocytosis. eLife *10*, e68627. https://doi.org/10.7554/eLife.68627.
34. Prashar, A., Bhatia, S., Gigliozzi, D., Martin, T., Duncan, C., Guyard, C., and Terebiznik, M.R. (2013). Filamentous morphology of bacteria delays the timing of phagosome morphogenesis in macrophages. J. Cell Biol. *203*, 1081–1097. https://doi.org/10.1083/JCB.201304095.
35. Lee, D.J., Cox, D., Li, J., and Greenberg, S. (2000). Rac1 and Cdc42 are required for phagocytosis, but not NF-kappaB-dependent gene expression, in macrophages challenged with Pseudomonas aeruginosa. J. Biol. Chem. *275*, 141–146. https://doi.org/10.1074/JBC.275.1.141.
36. Schlam, D., Bagshaw, R.D., Freeman, S.A., Collins, R.F., Pawson, T., Fairn, G.D., and Grinstein, S. (2015). Phosphoinositide 3-kinase enables

phagocytosis of large particles by terminating actin assembly through Rac/Cdc42 GTPase-activating proteins. Nat. Commun. *6*, 8623. https://doi.org/10.1038/NCOMMS9623.

37. Jaumouillé, V., Cartagena-Rivera, A.X., and Waterman, C.M. (2019). Coupling of β2 integrins to actin by a mechanosensitive molecular clutch drives complement receptor-mediated phagocytosis. Nat. Cell Biol. *21*, 1357–1369. https://doi.org/10.1038/S41556-019-0414-2.
38. Rengarajan, M., Hayer, A., and Theriot, J.A. (2016). Endothelial Cells Use a Formin-Dependent Phagocytosis-Like Process to Internalize the Bacterium Listeria monocytogenes. PLoS Pathog. *12*, e1005603. https://doi.org/10.1371/JOURNAL.PPAT.1005603.
39. Czuczman, M.A., Fattouh, R., Van Rijn, J.M., Canadien, V., Osborne, S., Muise, A.M., Kuchroo, V.K., Higgins, D.E., and Brumell, J.H. (2014). Listeria monocytogenes exploits efferocytosis to promote cell-to-cell spread. Nature *509*, 230–234. https://doi.org/10.1038/nature13168.
40. Blander, J.M., and Medzhitov, R. (2004). Regulation of phagosome maturation by signals from toll-like receptors. Science *304*, 1014–1018. https://doi.org/10.1126/SCIENCE.1096158.
41. Zanoni, I., Ostuni, R., Marek, L.R., Barresi, S., Barbalat, R., Barton, G.M., Granucci, F., and Kagan, J.C. (2011). CD14 controls the LPS-induced endocytosis of Toll-like receptor 4. Cell *147*, 868–880. https://doi.org/10.1016/J.CELL.2011.09.051.
42. Rasmussen, J.P., Sack, G.S., Martin, S.M., and Sagasti, A. (2015). Vertebrate epidermal cells are broad-specificity phagocytes that clear sensory axon debris. J. Neurosci. *35*, 559–570. https://doi.org/10.1523/JNEUROSCI.3613-14.2015.
43. Miesenböck, G., De Angelis, D.A., and Rothman, J.E. (1998). Visualizing secretion and synaptic transmission with pH-sensitive green fluorescent proteins. Nature *6689*, 192–195. https://doi.org/10.1038/28190.
44. Gray, M.A., Choy, C.H., Dayam, R.M., Ospina-Escobar, E., Somerville, A., Xiao, X., Ferguson, S.M., and Botelho, R.J. (2016). Phagocytosis Enhances Lysosomal and Bactericidal Properties by Activating the Transcription Factor TFEB. Curr. Biol. *26*, 1955–1964. https://doi.org/10.1016/J.CUB.2016.05.070.
45. Wilks, J.C., and Slonczewski, J.L. (2007). pH of the cytoplasm and periplasm of Escherichia coli: rapid measurement by green fluorescent protein fluorimetry. J. Bacteriol. *189*, 5601–5607. https://doi.org/10.1128/JB.00615-07.
46. Gautier, E.L., Shay, T., Miller, J., Greter, M., Jakubzick, C., Ivanov, S., Helft, J., Chow, A., Elpek, K.G., Gordonov, S., et al. (2012). Gene-expression profiles and transcriptional regulatory pathways that underlie the identity and diversity of mouse tissue macrophages. Nat. Immunol. *13*, 1118–1128. https://doi.org/10.1038/NI.2419.
47. Mass, E., Ballesteros, I., Farlik, M., Halbritter, F., Günther, P., Crozet, L., Jacome-Galarza, C.E., Händler, K., Klughammer, J., Kobayashi, Y., et al. (2016). Specification of tissue-resident macrophages during organogenesis. Science *353*, aaf4238. https://doi.org/10.1126/SCIENCE.AAF4238.
48. Kanther, M., Sun, X., Mühlbauer, M., MacKey, L.C., Flynn, E.J., Bagnat, M., Jobin, C., and Rawls, J.F. (2011). Microbial colonization induces dynamic temporal and spatial patterns of NF-κB activation in the zebrafish digestive tract. Gastroenterology *141*, 197–207. https://doi.org/10.1053/J.GASTRO.2011.03.042.
49. Rahman, M.M., and McFadden, G. (2011). Modulation of NF-κB signalling by microbial pathogens. Nat. Rev. Microbiol. *9*, 291–306. https://doi.org/10.1038/nrmicro2539.
50. Peters, D.T., Reifs, A., Alonso-Caballero, A., Madkour, A., Waller, H., Kenny, B., Perez-Jimenez, R., and Lakey, J.H. (2022). Unraveling the molecular determinants of the anti-phagocytic protein cloak of plague bacteria. PLoS Pathog. *18*, e1010447. https://doi.org/10.1371/JOURNAL.PPAT.1010447.
51. Lovewell, R.R., Collins, R.M., Acker, J.L., O'Toole, G.A., Wargo, M.J., and Berwin, B. (2011). Step-wise loss of bacterial flagellar torsion confers progressive phagocytic evasion. PLoS Pathog. *7*, e1002253. https://doi.org/10.1371/JOURNAL.PPAT.1002253.
52. Freeman, S.A., Vega, A., Riedl, M., Collins, R.F., Ostrowski, P.P., Woods, E.C., Bertozzi, C.R., Tammi, M.I., Lidke, D.S., Johnson, P., et al. (2018). Transmembrane Pickets Connect Cyto- and Pericellular Skeletons Forming Barriers to Receptor Engagement. Cell *172*, 305–317.e10. https://doi.org/10.1016/J.CELL.2017.12.023.
53. Benyoussef, W., Deforet, M., Monmeyran, A., and Henry, N. (2022). Flagellar Motility During E. coli Biofilm Formation Provides a Competitive Disadvantage Which Recedes in the Presence of Co-Colonizers. Front. Cell. Infect. Microbiol. *12*, 896898. https://doi.org/10.3389/FCIMB.2022.896898.
54. Khan, K.N., Fujishita, A., Kitajima, M., Hiraki, K., Nakashima, M., and Masuzaki, H. (2014). Intra-uterine microbial colonization and occurrence of endometritis in women with endometriosis†. Hum. Reprod. *29*, 2446–2456. https://doi.org/10.1093/HUMREP/DEU222.
55. Larsen, S.B., Cowley, C.J., and Fuchs, E. (2020). Epithelial cells: liaisons of immunity. Curr. Opin. Immunol. *62*, 45–53. https://doi.org/10.1016/J.COI.2019.11.004.
56. Juncadella, I.J., Kadl, A., Sharma, A.K., Shim, Y.M., Hochreiter-Hufford, A., Borish, L., and Ravichandran, K.S. (2013). Apoptotic cell clearance by bronchial epithelial cells critically influences airway inflammation. Nature *493*, 547–551. https://doi.org/10.1038/NATURE11714.
57. Bakkers, J., Kramer, C., Pothof, J., Quaedvlieg, N.E.M., Spaink, H.P., and Hammerschmidt, M. (2004). Has2 is required upstream of Rac1 to govern dorsal migration of lateral cells during zebrafish gastrulation. Development *131*, 525–537. https://doi.org/10.1242/DEV.00954.
58. Jessen, J.R. (2015). Recent advances in the study of zebrafish extracellular matrix proteins. Dev. Biol. *401*, 110–121. https://doi.org/10.1016/J.YDBIO.2014.12.022.
59. Chan, C.J., Costanzo, M., Ruiz-Herrero, T., Mönke, G., Petrie, R.J., Bergert, M., Diz-Muñoz, A., Mahadevan, L., and Hiiragi, T. (2019). Hydraulic control of mammalian embryo size and cell fate. Nature *571*, 112–116. https://doi.org/10.1038/S41586-019-1309-X.
60. Dragoš, A., Kiesewalter, H., Martin, M., Hsu, C.Y., Hartmann, R., Wechsler, T., Eriksen, C., Brix, S., Drescher, K., Stanley-Wall, N., et al. (2018). Division of Labor during Biofilm Matrix Production. Curr. Biol. *28*, 1903–1913.e5. https://doi.org/10.1016/J.CUB.2018.04.046.
61. Blanch-Asensio, M., Tadimarri, V.S., Wilk, A., and Sankaran, S. (2024). Discovery of a high-performance phage-derived promoter/repressor system for probiotic lactobacillus engineering. Microb. Cell Fact. *23*, 1–13. https://doi.org/10.1186/S12934-024-02302-7/FIGURES/6.
62. Fiore, A., Yu, G., Northey, J.J., Patel, R., Ravenscroft, T.A., Ikegami, R., Kolkman, W., Kumar, P., Dilan, T.L., Ruetten, V.M.S., et al. (2025). Live imaging of the extracellular matrix with a glycan-binding fluorophore. Nat. Methods *22*, 1070–1080. https://doi.org/10.1038/S41592-024-02590-2.
63. Tahinci, E., and Symes, K. (2003). Distinct functions of Rho and Rac are required for convergent extension during Xenopus gastrulation. Dev. Biol. *259*, 318–335. https://doi.org/10.1016/S0012-1606(03)00206-9.
64. Hanovice, N.J., McMains, E., and Gross, J.M. (2016). A GAL4-inducible transgenic toolkit for the in vivo modulation of Rho GTPase activity in zebrafish. Dev. Dyn. *245*, 844–853. https://doi.org/10.1002/DVDY.24412.
65. Roggo, C., Carraro, N., and van der Meer, J.R. (2019). Probing chemotaxis activity in Escherichia coli using fluorescent protein fusions. Sci. Rep. *9*, 3845. https://doi.org/10.1038/S41598-019-40655-X.
66. Ewels, P.A., Peltzer, A., Fillinger, S., Patel, H., Alneberg, J., Wilm, A., Garcia, M.U., Di Tommaso, P., and Nahnsen, S. (2020). The nf-core framework for community-curated bioinformatics pipelines. Nat. Biotechnol. *38*, 276–278. https://doi.org/10.1038/S41587-020-0439-X.
67. Love, M.I., Huber, W., and Anders, S. (2014). Moderated estimation of fold change and dispersion for RNA-seq data with DESeq2. Genome Biol. *15*, 550. https://doi.org/10.1186/S13059-014-0550-8.

68. Mootha, V.K., Lindgren, C.M., Eriksson, K.F., Subramanian, A., Sihag, S., Lehar, J., Puigserver, P., Carlsson, E., Ridderstråle, M., Laurila, E., et al. (2003). PGC-1alpha-responsive genes involved in oxidative phosphorylation are coordinately downregulated in human diabetes. Nat. Genet. *34*, 267–273. https://doi.org/10.1038/NG1180.

69. Uhlén, M., Karlsson, M.J., Hober, A., Svensson, A.S., Scheffel, J., Kotol, D., Zhong, W., Tebani, A., Strandberg, L., Edfors, F., et al. (2019). The human secretome. Sci. Signal. *12*, eaaz0274. https://doi.org/10.1126/SCISIGNAL.AAZ0274.

70. Dyer, S.C., Austine-Orimoloye, O., Azov, A.G., Barba, M., Barnes, I., Barrera-Enriquez, V.P., Becker, A., Bennett, R., Beracochea, M., Berry, A., et al. (2025). Ensembl 2025. Nucleic Acids Res. *53*, D948–D957. https://doi.org/10.1093/NAR/GKAE1071.

STAR★METHODS

KEY RESOURCES TABLE

REAGENT or RESOURCE	SOURCE	IDENTIFIER
Antibodies		
Mouse Monoclonal Anti-Oct3/4	Santa Cruz Biotechnology	Cat#sc-5279; RRID: AB_628051
Rabbit Monoclonal Anti-CDX2	Abcam	Cat#235R-15; RRID: AB_1516799
Donkey Polyclonal Anti-Mouse IgG Alexa Fluor 647	Jackson ImmunoResearch	Cat#715-605-151; RRID: AB_2340863
Donkey Polyclonal Anti-Rabbit IgG Alexa Fluor 488	Jackson ImmunoResearch	Cat#711-545-15;2 RRID: AB_2313584
Bacterial and virus strains		
BL21 (DE3) Chemically Competent *E. coli*	Invitrogen	Cat#C600003
E. coli (K-12 strain) BioParticles, Texas Red conjugate	Invitrogen	Cat#E2863
WBY003 (MG1655 *E. coli* bearing the F plasmid and expressing GFP, lacking IS1 upstream of the flhD promoter)	Lovewell[51]	N/A
MF001 (MG1655 bearing the F plasmid and expressing YFP)	Lovewell et al.[51]	N/A
mKate-expressing *B. subtillis*	Dragoš et al.[60]	N/A
mCherry-expressing *L. plantarum*	Blanch-Asensio et al.[61]	N/A
mCherry and GFP-expressing *S. aureus* (strain 132)	Eduard Torrents lab	N/A
mScarlett-expressing *P. aeruginosa* PAO1 (CECT 4122)	Admella J. et al. (2025), unpublished data	N/A
S. aureus (Wood strain without protein A) BioParticles, Alexa Fluor 488 conjugate	Invitrogen	Cat#S23371
Biological samples		
Donated human embryos	Dexeus Mujer Barcelona	N/A
Chemicals, peptides, and recombinant proteins		
SYTO 60 Red Fluorescent Nucleic Acid Stain	Invitrogen	Cat#S11342
UltraPure low-melting point Agarose	Invitrogen	Cat#16520100
SMIFH2	Sigma-Aldrich	Cat#S4826
CK666	Sigma-Aldrich	Cat#SML0006
LY-294,002 hydrochloride	Sigma-Aldrich	Cat#L9908
Dimethyl sulfoxide (DMSO)	Sigma-Aldrich	Cat#D8418
Dextran Alexa Fluor 647 10,000 MW	Invitrogen	Cat#D22914
Phalloidin Alexa Fluor 555	Invitrogen	Cat#A34055
LPS-EB	Invivogen	Cat#tlrl-eblps
Annexin V Alexa Fluor 488 conjugate	Invitrogen	Cat#A13201
Bodipy FL-C5 Ceramide	Invitrogen	Cat#D3521
Lysotracker RED DND-99	Invitrogen	Cat#L7528
Hoechst 33342	Invitrogen	Cat#H3570
Rhobo6	Fiore et al.[62]	N/A
Pregnant Mare Serum Gonadotropin (PMSG)	Biopyc, Foligon	N/A
Recombinant Human Chorionic Gonadotropin (hCG)	Farma Higiene, Chorulon	N/A
M2 medium	Sigma-Aldrich	Cat#M7167
KSOM Mouse Embryo Media	Sigma-Aldrich	Cat#MR-107

(*Continued on next page*)

Continued

REAGENT or RESOURCE	SOURCE	IDENTIFIER
Glass beads	Supelco	Cat#440345
DAPI Nucleic Acid Stain	Invitrogen	D1306
Phalloidin Alexa Fluor 568	Invitrogen	Cat#A12380
Oocyte/embryo thawing media	Kitazato	Cat#VT602
G-TL medium	Vitrolife	Cat#10145
SPY555-actin	Spirochrome	N/A
G-GAMETE medium	Vitrolife	Cat#10126
OVOIL mineral oil	Vitrolife	Cat#10029
Mineral oil	Sigma-Aldrich	Cat#M8410
Critical commercial assays		
mMESSAGE mMACHINE SP6 Kit	Invitrogen	Cat#AM1340
GeneJET PCR Purification Kit	Thermo Scientific	Cat#K0701
GeneJET Plasmid Miniprep Kit	Thermo Scientific	Cat#K0502
Deposited data		
RNAseq raw data 1.5 hours after injection of bacteria	CORA.RDR	CORA.RDR: https://doi.org/10.34810/data1201
RNAseq raw data 9 hours after injection of bacteria	CORA.RDR	CORA.RDR: https://doi.org/10.34810/data2009
Experimental models: Organisms/strains		
Zebrafish: AB wild-type		N/A
Zebrafish: Tg(*actb2:Lifeact-GFP*)		RRID: ZFIN_ZDB-TGCONSTRCT-130206-1
Zebrafish: Tg(*krt18:Gal4*)		RRID: ZFIN_ZDB-TGCONSTRCT-101028-1
Zebrafish: Tg(*krt18Gal4FF/UAS:Lifeact-GFP*)	Hoijman et al.[19]	N/A
Zebrafish: Tg(*actb2:Myl12.1-eGFP*)		RRID: ZFIN_ZDB-TGCONSTRCT-130108-2
Mouse: B6CBAF1/J	The Jackson Laboratory	RRID:IMSR_JAX:100011
Mouse: B6.Cg-Tg(CAG-DsRed*MST) 1Nagy/J1	The Jackson Laboratory	RRID:IMSR_JAX:006051
Mouse: B6.129(Cg)-Gt(ROSA) 26Sor$^{tm4(ACTB-tdTomato,-EGFP)Luo/J}$	The Jackson Laboratory	RRID:IMSR_JAX:007676
Mouse: B6.Cg-Ptprca Tg(UBCPA-GFP) 1Mnz/J	The Jackson Laboratory	RRID:IMSR_JAX:022486
Recombinant DNA		
Plasmid pTol2(UAS:FYVE-GFP)	Rasmussen et al.[42]	N/A
Plasmid Caf1	Peters et al.[50]	N/A
Plasmid dnRac1	Tahinci and Symes[63]	N/A
Plasmid pTol2(UAS:dnRac1-GFP)	Hanovice et al.[64]	N/A
Plasmid pHLuorin	Roggo et al.[65]	N/A
Software and algorithms		
ImageJ	N/A	https://imagej.nih.gov/ij/
Prism	GraphPad	https://www.graphpad.com/
Excel	Microsoft Office	https://www.microsoft.com/en-us/microsoft-365/excel
Adoble Illustrator	Adobe	https://www.adobe.com/products/illustrator.html
HiSeq 2500 Software version 2.2.58	Illumina	https://support.illumina.com/sequencing/sequencing_instruments/hiseq_2500/

(*Continued on next page*)

Continued

REAGENT or RESOURCE	SOURCE	IDENTIFIER
GSEA software version 4.3.2	Broad Institute	https://www.gsea-msigdb.org/gsea/index.jsp
Biorender	Biorender	https://www.biorender.com/
Other		
Holding pipettes	Vitrolife	Cat#15328
Microinjection pipettes	Vitrolife	Cat#15430
Glass bottom culture dishes 35 mm	MatTek	Cat#P35G-1.5-14-C
Eppendorf Femtojet 5247 microinjector	Eppendorf	N/A
Capillaries	Harvard Apparatus	Cat#EC1 30-0091
Eppendorf Cell Tram 4r Oil microinjector	Eppendorf	Cat#5196000030
Eppendorf Transferman 4r micromanipulator	Eppendorf	Cat#5193000020

EXPERIMENTAL MODELS

Zebrafish embryo work

AB wild-type zebrafish and the following transgenic lines were used: Tg(*actb2:Lifeact-GFP*), Tg(*krt18:Gal4*), Tg(*krt18:Gal4FF/UAS:Lifeact-GFP*) and Tg(*actb2:Myl12.1-eGFP*). Fish were maintained and bred according to the standard procedures at the aquatic facility of the Bellvitge Biomedical Research Institute (IDIBELL). Embryos were kept in E3 medium at 25°C–31°C prior to experiments and staged based on morphological criteria and hours post fertilization (hpf). All protocols used have been approved by the Ethical Committee of Animal Experimentation of IDIBELL and were implemented according to national and European regulations. Experiments were carried out in accordance with the principles of the 3Rs. Females were crossed with males (between 5-12 months of age) to obtain eggs.

Mouse embryo work

All protocols used have been approved by the Institutional Animal Care and Use Ethic Committee (PRBB–IACUEC) and Animal experimentation Ethic committee of the Barcelona Scientific Park-Òrgan Habilitat (CEEA-PCB-OH) and conform to the guidelines from the European Community Directive and Spanish legislation for the experimental use of animals. Mouse lines were maintained and bred according to the standard procedures at the rodent facility of the Parc de Recerca Biomèdica de Barcelona (PRBB) and IBEC. Mice were housed in IVCs (Individually Ventilated Cages) in an SPF unit following local regulations. Ambient temperature was maintained between 20-24°C, ambient humidity ranged between 40-70% and they were kept in a 12 h light/dark cycle.

Embryos were isolated from B6CBAF1, B6.Cg-Tg(CAG-DsRed*MST)1Nagy/J1, and B6.129(Cg)-Gt(ROSA)26Sor$^{tm4(ACTB-tdTomato,-EGFP)Luo}$/J; B6.Cg-Ptprc^{a} Tg(UBCPA-GFP)1Mnz/J strains. Superovulated females (4-12 weeks old) were mated with male mice (8-24 weeks old). Female superovulation was induced by intraperitoneal injection of 5 international units (IU) pregnant mare's serum gonadotropin (PMSG, Biopyc, Foligon), followed by intraperitoneal injection of 5 IU human chorionic gonadotropin (hCG, Farma Higiene, Chorulon) 47 h later. 0.5 or 2.5 days post coitum (dpc), embryos were flushed from oviducts with M2 medium (Sigma-Aldrich) and cultured in KSOM (Sigma-Aldrich) at 37°C and 5% CO2 covered by mineral oil (Sigma-Aldrich).

Human embryo work

Donated human blastocysts were obtained from Dexeus Mujer, Barcelona. All blastocysts were de-identified prior to the thawing process. They were cryopreserved and donated to research following the Spanish law 14/2006 of human assisted reproduction. All donating couples received an informative letter about the project and signed an informed consent. Confidentiality will follow the European Data protection policy 2016/679, April 27th, 2016, the Spanish organic law 3/2018 of December 5th (LOPDGDD), the Spanish law 14/2007 of biomedical research, and the declaration of Helsinki (last version Fortaleza, Brazil 2013). The procedure for experimentation with donated human embryos was approved by the Ethical Committee of Regenerative Medicine Research of IDIBELL, The Ethical Committee of clinical research of Grupo Hospitalario Quirón (Dexeus Mujer), the Spanish Guarantee Commission for the Donation and Use of Human Cells and Tissues, and the Department of Health, Government of Catalonia.

METHOD DETAILS

Expression of proteins in zebrafish embryos

For staining of subcellular components or interferences, the following mRNAs encoding fusion proteins were synthetized from pCS2+ plasmids using the SP6 mMessenger mMachine kit (Invitrogen) and injected at 1-cell stage: gpi-gfp and lyn-tdtomato (50 pg, plasma

membrane staining), dominant negative Rac1N17[63] (dnRac1, 20 pg) and dominant negative Fhod1 (dnFhod1, 20 pg, a gift from Verena Ruprecht). For generating the dnFhod1 construct, the GBD/FH3 domain of Fhod1 was cloned into the pCS2+ plasmid. The dnRac1 was also injected at the 16-cell stage to generate mosaic embryos with individual cells expressing the protein. Cells expressing dnRac1 were identified by the co-expression of the H2A-mCherry protein, as both mRNAs co-segregate.[19] To express FYVE-GFP or dnRac1-GFP specifically in the EVL, the Tg(*krt18:Gal4*) line was injected with 50 pg of plasmid DNA of UAS:FYVE-GFP[42] or 25 pg of plasmid DNA of UAS:dnRac1-GFP,[64] together with 25 pg of Tol2 transposase mRNA at 1-cell stage.

Bacterial strains

Bacteria expressing the following fluorescent proteins were used: mCherry-, GFP- or Cerulean-expressing NZY5α *E. coli* (a gift from Javier Santos Moreno, Universitat Pompeu Fabra, Spain), mTagBFP2 BL-21 *E. coli*, pHLuorin[62]-expressing BL-21 *E. coli*, CAF1[50]-expressing BL-21 *E. coli*, fixed *E. coli* particles (BioParticles™ Texas Red conjugate, Invitrogen), WBY003 (MG1655 *E. coli* bearing the F plasmid and expressing GFP, lacking IS1 upstream of the flhD promoter) as low motility bacteria (Mot^{LOW}), MF001 (MG1655 bearing the F plasmid and expressing YFP) as highly motile bacteria (Mot^{HI}),[51] GFP- or mKate-expressing *B. subtillis*,[60] mCherry-expressing *L. plantarum*,[61] mCherry- or GFP-expressing *S. aureus* 132, mScarlett-expressing *P. aeruginosa* PAO1 (CECT 4122) and Alexa Fluor 488-conjugated fixed *S. aureus* (Invitrogen). For time-lapse experiments, mCherry-expressing *S. aureus* were pre-stained with SYTO 60 red fluorescent nucleic acid stain (Invitrogen) to ensure optimal visualization through time. The plasmids mentioned were introduced into chemically competent bacteria by standard heat-shock transformation procedures. Fixation of bacteria was performed by incubation in 4% paraformaldehyde (PFA) for 60 min.

Puncturing experiments in zebrafish embryos

To allow the infiltration of bacteria inside the zebrafish embryo, a needle of about 80 μm external diameter was introduced laterally through the EVL about 200 μm inside dechorionated embryos, maintained for 5 seconds, and removed slowly to avoid creating a large deformation in the embryonic surface. This perturbation created a hole in the epithelial surface. Individual embryos were then submerged in 500 ul of Danieau's solution with *E. coli* at a concentration of $2x10^9$ CFUs (colony forming units)/ml for 30 minutes. After two washes in Danieau's solution, the punctured embryos were mounted in agarose to perform live imaging 1 hour after damage. For the survival experiments in normal or germ-free medium, embryos were dechorionated at dome stage, punctured and subsequently maintained in either fish water (collected from the zebrafish housing system) or germ-free water (fish water supplemented with 250 ng/ml amphotericin, 5 μg/ml kanamycin, and 100 μg/ml ampicillin, pre-incubated for 2 h). Phenotypes were classified as described below. To confirm the presence of bacteria in the fish water, 20 μl of the sample were plated onto an agar plate containing LB medium without antibiotics.

Injection of bacteria into zebrafish embryos

Cultures of bacteria in Luria Broth (LB, *E. coli* and *P. aeruginosa*), Tryptic Soy Broth (TSB, *S. aureus*) or Man, Rogosa and Sharpe (MRS, *L. plantarum*) medium with the following antibiotics were prepared: *S. aureus* expressing mCherry or GFP, *E. coli* expressing mCherry, Cerulean or GFP, *E. coli* expressing pHLuorin and CAF1, and WBY003, 10 μg/ml of ampicillin; MF001, 50 μg/ml of kanamycin; *L. plantarum*, 10 μg/mL of erythromycin and *B. subtillis*, 10 μg/mL of chloramphenicol. 500 ul of the ON culture were centrifuged at 6.800 g for 2 min and then resuspended in 50 ul of LB or PBS (Phosphate-Buffered Saline). In the latter case, 2 washes were performed to eliminate the LB. Bacterial culture concentration was adjusted measuring the optical density and plating the bacteria on solid LB to calculate the CFUs for injection into the embryo. Using an Eppendorf Femtojet device 5247, 0.5 nl of the bacterial suspension (5,000 CFUs) were injected into the embryo interior, in close proximity to the EVL layer, at dome stage. For the phagocytosis saturation curve, dilutions of bacteria were prepared in PBS to inject the same volume with varying numbers of bacteria.

Developmental defects and survival experiments

For puncturing or injection experiments, analysis and classification of the phenotypes were performed at 24 hpf (19 hours after bacterial challenge). Embryos were classified according to the following scale: normal (no defect or delay detected), slightly affected (small delay in development-subtle anomalies), severely affected (large delay in development, lack of whole structures, severe deformations), and dead (chorions with degraded material inside or small fragments of embryos).

Live imaging of zebrafish embryos

Embryos were maintained in E3 medium (5 mM NaCl, 0.17 mM KCl, 0.33 mM $CaCl_2$, 0.33 mM $MgSO_4$) until they were dechorionated and mounted in 1% low-melting point agarose in Danieau's solution (58 mM NaCl, 0.7 mM KCl, 0.4 mM $MgSO_4$, 0.6 mM $Ca(NO_3)$, 2.5 mM HEPES) over 35 mm glass bottom dish (MatTek) and imaged with a 20x glycerol- or 40x oil- immersion objectives at 28°C on Leica TCS SP5, or Zeiss 980 confocal microscopes. Laser excitation of 405 nm, 476 nm, 488 nm and 561 nm were used. z-stacks of 0.5-2 μm spacing between z-slices were acquired with a temporal resolution of 1 s-20 min depending on the experiment. Software used were Zen 2.1. SP3 (v14.0.12.201) and LAS AF (v2.7.3.9723). Embryos from experiments with pathogenic bacteria were imaged in a Zeiss 780 confocal microscope.

The ratiometric analysis of the fluorescence from the pHLuorin reporter was performed by sequentially exciting the sample with 405 nm and 476 nm laser lines. Emission was detected in both cases at 493–595 nm. The ratio of emission at 405/476 was then calculated for single bacteria. The signal from excitation at 405 and 476 nm are shown in red and green, respectively.

For capturing protrusion dynamics at the tissue and single cell level, high speed 4D timelapse imaging was performed with the Zeiss 980 confocal microscope, acquiring 17 Z-sections every 5 seconds. The expression of Lifeact-GFP only in EVL cells using the Tg(*krt18:Gal4FF/UAS-Lifeact-GFP*) line allowed us to visualize specific subcellular dynamics. For the study of protrusion dynamics in presence of CK666 and SMIFH2, timelapse imaging was performed acquiring 20 Z-sections every 83 seconds in Tg (*actb2:LifeactGFP*) embryos for 45 minutes.

Simultaneous detection of apoptotic cells and bacterial ingestion

Embryos were injected with H2A-mCherry mRNA at one-cell stage to detect ingestion of apoptotic particles. The expression of H2A-mCherry did not affect phagocytic uptake (Figure S2A).[19] At the blastula stage, embryos were injected with cerulean *E. coli* and imaged after 1 h to count the number of EVL cells having phagocytosed both apoptotic particles and bacteria.

Interference treatments in zebrafish embryos

Dechorionated embryos were preincubated with 50 μM SMIFH2 (Sigma-Aldrich), 100 μM CK666 (Sigma-Aldrich), 100 μM LY294 (Sigma-Aldrich) or DMSO (control) for 1 h in Danieau's solution, injected with bacteria, mounted including the corresponding drugs in the agarose, and imaged 1 h after injection (hai). For the study of phagocytic cup formation in the presence of CK666 and SMIFH2, Tg(*actb2:Lifeact-GFP*) embryos were incubated in the same conditions and the time-lapse imaging of the EVL performed right after mounting. Images of the internal embryonic cells were also acquired to control for Actin organization. For evaluation of EVL identity in presence of the drugs, Tg(*krt18:Gal4FF/UAS:Lifeact-GFP*) embryos were incubated with SMIFH2, CK666, or DMSO for 4 h in Danieau's solution, and then imaged to detect the Lifeact-GFP EVL-specific signal. For EVL barrier function analysis, embryos were preincubated with SMIFH2, CK666 or DMSO in Danieau's solution for 2 h before incubating them for an additional 1.5 h in presence of 1 mg/ml Dextran 10,000 MW, AF647 (Invitrogen) and then imaged in solution.

Embryos expressing dnRac1-GFP only in the EVL were injected with bacteria at 30% epiboly stage, fixed 1 h later in 4% PFA ON, and stained with Phalloidin AF555 (Invitrogen) before confocal imaging. For LPS experiments with *E. coli* and *S. aureus*, 5mg/ml LPS-EB (InvivoGen) were included in the bacterial suspension to have a final LPS concentration of 4 mg/ml in the bacterial mix just before injection. To obtain the phagocytosis curve upon different concentrations of LPS, bacteria were resuspended in different concentrations of LPS diluted in PBS: 0.2 mg/ml, 0.8 mg/ml and 4 mg/ml. For Annexin V experiments, bacteria were resuspended in Annexin V Alexa Fluor 488 conjugate (Invitrogen) before injection.

Analysis of the vesicular transit after bacterial ingestion in zebrafish embryos

Plasma membrane was stained by injecting 1-cell stage AB embryos with Bodipy FL-C5 Ceramide (Invitrogen). To stain for early phagosomes, FYVE-GFP was expressed specifically in EVL cells (see above). To observe the phagosomes at 16 hpf (11 hai), embryos were incubated overnight at 23°C to slow down the development and imaged when they corresponded to 16 hpf stage. To stain for lysosomes at 16 or 24 hpf, embryos were incubated with 0.2 μM Lysotracker RED DND-99 (Invitrogen) for 2 h.

Clearance experiments of CAF1-expressing *E. coli* in zebrafish embryos

1 nl of bacterial cultures of *E. coli* expressing CAF1 or pHLuorin (used as a control, as they were phagocytosed normally, and both are BL21-derived strains) was injected into embryos at the dome stage at comparable CFUs for each strain (600-900 for pHluorin-expressing bacteria, and 150-300 for CAF1-expressing bacteria). Before injection, bacteria were stained with Hoechst 33342 (Invitrogen) 1 μg/mL for 15 min, and then collected by centrifugation at 6.800 g, washed 3 times in PBS and finally resuspended in 50 ul of PBS to be injected. pHluorin-expressing *E. coli* with the same staining was used as a control. In the images from these experiments, the nuclei of the embryonic cells were partially stained by the Hoechst from the bacteria, and therefore these nuclei were pseudocolored in the figure. A control injecting the flocculent layer where the CAF1 protein accumulates (without bacteria) was performed.

Bacterial motility experiments in zebrafish embryos

Mot^{HI} and Mot^{LOW} bacteria expressing YFP and GFP respectively, were mixed at equal concentrations and injected at dome stage at different distances from the EVL. To clearly distinguish both fluorescent signals and correctly identify the identity of each bacterium, an excitation laser of 476 nm was used to only excite the GFP protein (detector 484-521 nm, green channel), and an excitation laser of 514 nm was used to excite both the GFP and YFP proteins (detector 523-558 nm, red channel). Therefore, the Mot^{LOW} bacteria were represented as an overlay of the green and red channels (white) and the Mot^{HI} bacteria only in the red channel. The motility of each strain was checked by semi-solid agar assays. Staining with Rhobo6[62] was performed by injecting 5 nl inside the embryo at dome stage (for early embryos) or incubating for 2 h in a 5 μM solution of the dye (for larval stage). Embryos were then mounted for live imaging.

Phagocytosis assays in other epithelia

Tricaine anesthetized Tg(*actb2:Myl12.1-eGFP*) zebrafish embryos were injected at 24 hpf with 0.5 nl of mCherry-expressing *E. coli* bacteria (approximately 5,000 CFUs) into the lumen of the otic vesicle, and were mounted in agarose and imaged after 6 h of injection. 5 days post-fertilization *Tg(actb2:Myl12.1-eGFP)* larvae were incubated in E3 including Bodipy 10 μM FL-C5 (Invitrogen) to distinguish the intestine lumen together with mCherry-expressing *E. coli* at a concentration of $2x10^9$ CFUs/ml. 6 h later, larvae were mounted in agarose with tricaine and imaged.

RNAseq experiments

Tg(*krt18:Gal4FF/UAS:Lifeact-GFP*) embryos expressing an EVL-specific GFP were injected with mCherry-expressing *E. coli* (bacteria group) or PBS (control group) at dome stage. For the experiment at 1.5 h post-injection the embryos were mechanically ruptured after this time to prepare embryonic cell suspensions. The cells from the bacteria group were FACS sorted for the GFP and mCherry signal, enriching the sample in EVL ingesting or in contact with bacteria. The cells from the control group were sorted by the GFP signal of EVL cells from PBS injected embryos. For the experiment at 9 h post-injection, embryos were incubated for 1 h at 28°C right after bacterial injection and then incubated at 23°C overnight to slow down development. The following day the embryos were staged, dechorionated and mechanically ruptured at 14 hpf to prepare embryonic cell suspensions. The cells from both groups were FACS sorted for the GFP signal. RNA from the recovered cells was prepared using the RNAeasy micro kit from QIAGEN. Illumina libraries were prepared using the SMARTseq_protocol NEBNextUltra_mRNA and sequenced on a HiSeq2500 v4 to produce 50-nt single end reads, controlled by the HiSeq control software v2.2.58. The raw RNA sequencing data were aligned to the zebrafish genome (GRCz10) using the RNAseq pipeline (https://github.com/nf-core/rnaseq) deposited in the nf-core framework.[66] The version of the pipelines used in the analysis was 3.10.1. The resulting gene expression matrices were further analyzed to find differentially expressed genes with the R library DESeq2 (v1.36.0).[67] Gene set enrichment analysis was computed using the GSEA software (version 4.3.2)[68] with a manually curated set of NF-κB pathway's genes based on https://www.bu.edu/nf-kb/gene-resources/target-genes/. For the GO analysis, the Gorilla application was used. The lists of secreted proteins has been obtained from the Human Protein Atlas repository (proteinatlas.org, v24).[69] Previously, human genes have been converted to zebrafish orthologous genes by using Ensembl Biomart.[70]

Mouse embryo injection experiments

Using an inverted Olympus IX71 microscope with an Eppendorf Cell Tram 4r Oil microinjector and Eppendorf Transferman 4r micromanipulators, about 20-40 bacteria were injected into the blastocoel of E3.5 embryos. 5-10 glass beads (9-13 μm (Supelco)) were or not coated with Texas Red-conjugated fixed *E. coli* (Invitrogen) by agitation for 3 h at 37°C, washed in PBS and injected similarly to the fixed bacteria.

The embryos were imaged 1 hai to check the proper localization of the injected bacteria. Live mouse embryos were imaged in KSOM medium with a 20x water immersion objective on a Zeiss 780 confocal microscope equipped with an incubation chamber to keep the samples at 37°C and 5% CO2. The fluorescent signals from the embryos or the bacteria were properly identified using excitation/detection at 514 nm/553-590 nm for membrane-TdTomato or cytoplasmic DsRed, and 594 nm/621-735 nm for Texas Red. z-stacks were acquired for each embryo at different times after injection.

For the bacterial ingestion experiments in the presence of the CK666 drug, the same protocol was followed but injections of bacteria were performed in a KSOM drop containing CK666 at 250 uM. For the control group the same volume of DMSO was added in the KSOM drop. The blastocysts were incubated in a KSOM drop with the same CK666 concentration for 7 h, fixed after this time in 4% PFA for 1 h and stored overnight in 0.25% X-100 Triton in PBS. The following day embryos were stained with Phalloidin AF555 (Invitrogen) at 33 nM in 0.25% X-100 Triton in PBS for 1 h. Subsequently, blastocysts were washed twice in 0.1% X-100 Triton in PBS (PBS-T) and mounted on glass-bottom dishes for imaging.

Mouse embryo immunostaining

Embryos were fixed in a solution containing 10% formalin, 0.1% Tween, and 0.01% X-100 Triton for 15 minutes, 7 hai. Following fixation, embryos were washed three times in PBS-T and stored at 4°C. For immunostaining, embryos were sequentially incubated in the following solutions: Permeabilization buffer (PBS + 0.5% Triton) for 15 minutes at room temperature (RT), Blocking buffer (10% BSA in PBS-T) for 45 minutes at RT, Primary antibody (AB) buffer (1:10 blocking buffer + primary antibodies) overnight at 4°C, and Secondary AB buffer (1:10 blocking buffer + secondary antibodies, DAPI, and Phalloidin) for 1 h and 30 min at 4°C. After each incubation step, embryos were washed in PBS-T. The primary antibodies used were Oct4 (1:200, Santa Cruz, sc-5279) and CDX2 (1:500, Abcam, ab76541). The secondary antibodies used were AF647 (1:500, Jackson, 715-605-151) and AF488 (1:500, Jackson, 711-545-152). Phalloidin AF568 (1:200, Invitrogen, A12380) and DAPI (1:200, Invitrogen, D1306) were also included in the staining protocol.

Human embryo injection experiments

Human embryo procedures were performed at the Stem Cell Bank from IDIBELL. Vitrified embryos were thawed according to the manufacturer's protocol (VT602, Kitazato) and cultured for 2 h in individual drops of 50 ul of G-TL (Vitrolife) medium covered with OVOIL mineral oil (Vitrolife) in an incubator at 37°C and 6% CO2. They were left to re-expand for 2 h and then stained with SPY555-Actin in G-TL medium (1:2000, Spirochrome) for another 2 h. Using an inverted Olympus IX71 microscope and an Eppendorf Cell Tram 4r Oil microinjector, 15-20 Texas Red- or Alexa Fluor 488-conjugated fixed *E. coli* or 20-30 Alexa Fluor 488-conjugated fixed *S. aureus* were injected into the blastocoele in GAMETE medium (Vitrolife). Holding (Vitrolife) and microinjection (Vitrolife) pipettes were used to manipulate the embryo. Embryos were then incubated in G-TL medium for different times. Live imaging of human embryos was performed in a Zeiss 980 confocal microscope equipped with a chamber to maintain conditions of 37°C and 6% CO2, using a 25x times water-immersion objective. Excitation was performed at 561 nm, and detection at 563-584 nm for SPY555 and 614-755 nm for Texas red.

QUANTIFICATION AND STATISTICAL ANALYSIS

Image analysis and quantification

Raw data were analyzed and quantified using FIJI software (ImageJ 1.52p). Images were processed for figure preparation by applying Gaussian blur filter. In some cases, maximum z-projections or 3D reconstructions generated with the 3D viewer plugin are shown as indicated. Quantification of phagocytic activity was done using the Point Tool from z-stacks of images parallel to the embryonic surface. Individual bacteria were identified manually along the z-stack and classified as ingested (when located in the cell interior) or not by surface epithelial cells. Reslice of cross sections perpendicular to the embryonic surface were visualized to unequivocally assign the location of the bacteria. Bacteria were considered ingested when it was possible to visualize the GPI-GFP or MyosinII-GFP green signal of the basal epithelial plasma membrane underneath the signal of the fluorescent bacteria. Ingestion was quantified in 15-25 EVL cells per embryo that initially were close to injected bacteria. Either the whole epithelial area imaged or regions of it were used for quantification of phagocytic efficiency.

Dynamics of bacterial ingestion

For quantification of the dynamics of ingestion at the tissue level (Figure 1H), a region comprising 30 EVL cells was selected, and followed over time. To determine the clearance of bacteria from the embryo interior (Figures 1H and S4G), threshold and binary processing of a Z-projection from 3 slices was applied to the bacterial mCherry signal, and the number of pixels counted to estimate the area occupied by the non-ingested bacteria. This area was measured 3-4 μm deeper in the embryo interior with respect to the basal plasma membrane of the EVL.

To obtain the map of the spatial distribution of bacterial ingestion, the number of bacteria ingested by each EVL cell was quantified 45 minutes after injection, and color coded according to the 4 groups indicated in the figure. Each cell was then backtracked in time to identify its initial position. The cells shown in the map correspond to those at 0 min. The mCherry signal from non-ingested bacteria present inside the embryo right after injection was represented in black. To evaluate the spatial correlation of the initial availability of bacteria with the final location where bacteria were ingested (Figure 1J), groups of 4 cells were followed over the time lapse. The availability of bacteria for ingestion under each group of 4 cells was quantified by measuring the area occupied by the bacterial mCherry signal as explained above. At 45 minutes, the number of bacteria ingested by each group of 4 cells was counted, and the initial mCherry area in the 4 cells region was plotted against the final number of bacteria ingested by the group of EVL cells.

Fluorescence intensity profiling and kymograph analysis

To quantify the relative spatial distribution of the different fluorescent signals (i.e. Lifeact-GFP and bacterial mCherry), plot profiles were obtained by drawing a 5 μm line perpendicular to the long axis of the bacterium. To align the signals from different events, the maximal intensity of the fluorescent signal from the bacteria was located at the half of the distance between the positions corresponding to the 50% intensity. Fluorescence corresponding to Lifeact-GFP, Bodipy FL-C5, FYVE-GFP and Lysotracker DND-99 were quantified. A kymograph was generated using the reslice function along a linear selection parallel to the bacterial long axis.

Single cell quantification of ingestion in embryos expressing dominant-negative proteins

For the dnRac1 mosaic experiments, the red fluorescence signal from the co-expressed H2A-mCherry protein within the same cell was quantified, as the mRNA co-segregate but H2A-mCherry does not interfere with phagocytosis (Figure S2A).[19] Cells were considered H2A-mCherry+ when presented a red fluorescence signal greater than 20% of the maximum measured. For the dnRac1-GFP EVL-specific expression experiments, cells were considered dnRac1-GFP positive when the GFP signal was higher than the background fluorescence inside the embryo. For the dnFhod1 experiments, the red fluorescence signal from the co-expressed H2A-mCherry protein within the same cell was quantified. The red signal was normalized to the maximum H2A-mCherry signal obtained from all embryos. Only cells with bacteria ingested at or below the EVL were considered for quantification.

Dynamics quantification of phagocytic cup number

For the quantification of the number of phagocytic cups in presence of CK666 or SMIFH2, individual phagocytic cups engulfing bacteria were identified in 4D movies of from an area of 100x200 μm. Only actin that unequivocally wraps around a bacterium in the 3D visualization of the structure, and progressing over time, was considered a cup.

Ratiometric measurement of pHLuorin fluorescence in single bacteria

The fluorescence intensity from the pHLuorin sensor excited at each wavelength was estimated from the mean value obtained from a linear region covering single bacteria, and the ratio between both signals calculated.

Quantification and distribution analysis of Mot^{HI} and Mot^{LOW} bacterial ingestion

To estimate the ingestion of Mot^{HI} and Mot^{LOW} at the tissue level (Figure 5C), the number of bacteria ingested by 20 cells per embryo were counted. To analyze the single cell distribution (Figure 5D) of both bacteria, cells ingesting at least 1 Mot^{HI} bacterium were selected, and the difference between ingested Mot^{HI} and Mot^{LOW} bacteria was calculated for each individual cell. To visualize the

difference in ingested bacterial populations depending on the injection site (close to the EVL or 2–3 layers beneath the EVL), cells that had ingested at least 1 Mot^{HI} bacterium were selected, and among these, the number of cells that had also ingested at least one Mot^{LOW} bacterium was counted (Figure S5H).

Quantification of bacterial ingestion by mouse and human trophectoderm

To identify the bacteria ingested by the mouse or human trophectoderm, the z-stack of each embryo was analyzed slice by slice for the presence of fluorescent bacteria. Their location inside the trophectoderm was confirmed by reslicing the z-stack from each embryo, to have an orthogonal visualization plane. In most experiments trophectoderm and inner cell mass cells were distinguished by morphological characteristics, which was confirmed by immunostaining of Cdx2 (trophectoderm) and Oct4 (inner cell mass). In some cases, maximum z-projection of these images were finally generated to show the cell contour. The ingestion rate was calculated from the ratio of ingested/non-ingested bacteria (Figure 6D). The ingestion of coated or non-coated beads was calculated by counting the number of ingested beads per embryo in both groups. To quantify the rate of particles ingested by the trophectoderm (TE) or the inner cell mass (ICM), percentages for each embryo were calculated dividing the number of particles ingested by the TE or the ICM by the total number of particles ingested (Figure S6B). To differentiate between apoptotic particles or bacterial ingestion, cells were analyzed one by one to capture possible cases of coexistence inside the same cell of the DAPI and bacterial fluorescent signal. To quantify the percentage of particles ingested per embryo when treated or not with CK666, the rate of each embryo was calculated by dividing the number of particles ingested by the total number of particles injected into the embryo.

Statistics and reproducibility

Two-tailed Student t-tests were performed to evaluate statistical differences between the means using GraphPad Prism v10. Chi-squared test was used to compare differences in the proportions between groups. Mean, standard errors of the mean (SEM) and box plots were generated using GraphPad Prism v10 or Excel 2403 (Microsoft). A linear regression was performed using GraphPad Prism v10. For all data presented, independent experiments were repeated at least 3 times with similar results.

Sample sizes were chosen empirically to optimize the maximum number of samples per each experiment while also considering the 3Rs (reduction/ refinement/ replacement) for animal research and the experimental limitations such as the number of embryos possible to image simultaneously during *in vivo* acquisitions. At least 5 different embryos were analyzed for each experimental condition. Statistical tests were applied to evaluate the significance of the analyzed effects for the given sample sizes. Blinding was not required during data collection as standardized experimental procedures and imaging protocols were applied for different groups. Blinding during data analysis was applied when possible, involving multiple investigators with blinded datasets. Randomization was performed by using multiple parental couples for mating in each independent experiment, and randomly distributing embryos into different groups. Sex of the embryos used is naturally randomized as it was not determined due the early stages of development utilized.

Graphical illustrations and abstract design

All methodological diagrams and workflow schematics were created using BioRender (https://biorender.com).